photonics

IMPACT FACTOR 1.9

CITESCORE 3.5

Review

Quantum-Empowered Fiber Sensing Metrology

Xiaojie Zuo, Zhangguan Tang, Boyao Li, Xiaoyong Chen and Jinghua Sun

Special Issue
Quantum High Precision Measurement

Edited by
Dr. Anshou Zheng and Dr. Jibing Liu

MDPI

https://doi.org/10.3390/photonics12080763

photonics

MDPI

Review

Quantum-Empowered Fiber Sensing Metrology

Xiaojie Zuo, Zhangguan Tang, Boyao Li *, Xiaoyong Chen and Jinghua Sun

School of Electrical Engineering & Intelligentization, Dongguan University of Technology, Dongguan 523808, China

* Correspondence: liby@dgut.edu.cn

Abstract

Quantum sensing leverages quantum resources to enable ultra-precise measurements beyond classical limits, driving transformative advancements in metrology. Optical fiber quantum sensing, integrating optical fiber sensing with quantum technologies, enhances measurement precision and sensitivity from multiple perspectives, such as exploring high-sensitivity optical fiber sensing installations and generating high-quality optical fiber quantum states. Following decades of comprehensive investigations and remarkable advances in optical fiber quantum sensing technology, this review systematically examines research achievements in this field through two complementary perspectives: one is the basic principle of generating optical fiber quantum states and their applications in sensing and the other is optical fiber quantum interferometers and their applications in sensing. Finally, examine current opportunities and challenges as well as the future development of optical fiber quantum sensing.

Keywords: optical fiber sensing; quantum states; optical fiber quantum interferometers; sensitivity

1. Introduction

Optical fiber sensors offer several significant benefits, including their compact size, ease of operation, immunity to electromagnetic interference, and high reliability [1–3]. They are commonly utilized for precise measurements of pressure [4], temperature [5], refractive index [6], strain [7], and curvature [8,9] and find extensive applications in medicine, aerospace, manufacturing, and national defense. The working principle of optical fiber sensing technology is that when light is transmitted to the sensing element, the optical fiber sensor is affected by the measured external parameters (such as temperature, refractive index, strain, etc.), causing the light wave parameters (intensity, wavelength, frequency, phase, etc.) in the optical fiber to be modulated. After modulation, the signal is then sent to a detector for conversion, and the processing system analyzes the signal to extract information about the external parameter being measured, fulfilling the sensing function. By leveraging the fact that the properties of light in optical fibers are altered by external factors, a variety of types of sensors with excellent sensing capabilities can be developed and successfully commercialized.

Elevating measurement sensitivity opens new pathways to decoding fundamental natural phenomena while identifying faint signals or nanoscale materials that remain indetectable with standard approaches (for example, gravitational waves [10,11], weak magnetic field [12], charge [13]). There is no doubt that the precision of optical fiber sensing in the classical field is limited by the shot noise limit (SNL): $\frac{1}{\sqrt{N}}$, where N represents the

check for updates

Received: 11 June 2025
Revised: 9 July 2025
Accepted: 21 July 2025
Published: 29 July 2025

Citation: Zuo, X.; Tang, Z.; Li, B.; Chen, X.; Sun, J. Quantum-Empowered Fiber Sensing Metrology. *Photonics* **2025**, *12*, 763. https://doi.org/10.3390/photonics12080763

count of repeated measurements and, when detecting physical quantities with a light field, N is the fluctuation in the number of photons in the detection beam. Its presence causes signals that are weaker than its amplitudes of noise to go undetected. The advent of lasers has enabled the rapid development of quantum optical technology. Quantum sensing, through quantum systems, utilizes quantum properties (such as quantum entanglement, quantum coherence, and squeezed states) to achieve measurement precision break through the SNL, significantly enhancing the sensitivity and precision of quantum sensors [14–19]. As a result, it can be extensively utilized in areas such as gravitational wave detection [20,21], microscopy [22], and biological detection [23]. Although quantum sensing has prospects and advantages in many aspects, the vast majority of research is still at the stage of principle and experimental demonstration, lacking mature and easily exercisable practical applications. The integration of quantum technology with optical fiber sensing is anticipated to usher in a new era for the real-world use of quantum sensing technology. The optical parametric amplifier based on the second-order nonlinear effect ($\chi^{(2)}$) of nonlinear crystals is an effective device to generate quantum light sources [24–26]. Although the third-order nonlinear effect ($\chi^{(3)}$) in optical fibers is much weaker than the second-order nonlinear effect ($\chi^{(2)}$), optical fibers have the advantage of a long nonlinear action length. Therefore, the third-order nonlinear effect ($\chi^{(3)}$) in optical fibers can also generate quantum light sources. In addition, the Kerr effect in optical fibers can generate the polarized squeezed light [27–29]. Quantum light sources generated by optical fibers can be well effectively coupled with high-performance optical fiber couplers, filters, and polarization control devices. This integration minimizes optical loss during the quantum sensing implementation, promoting the miniaturization and practical use of quantum light sources.

By utilizing the property of light transmitted through optical fibers, which can be easily influenced by external factors, a variety of sensors with excellent sensing capabilities can be created [30–33]. According to the working principle, they can be classified into two types. One is the incoherent sensor: there is no interference effect of light in the structure [34,35] and the measured physical quantity directly changes the parameters of light. Another type is the coherent optical fiber sensor: there is an interference effect of light in its structure. A variation in the measured physical quantity will affect the interference properties of the light. The output light field of the interferometer contains all the information such as the frequency, phase, and amplitude of the detected light field, and its signal-to-noise ratio (SNR) is higher than that of direct measurement. The coherent-type optical fiber sensor is an effective sensing tool. Most quantum sensing systems and optical fiber sensing installations are constructed based on interferometers (Sagnac interferometer [36,37], Mach-Zehnder interferometer [19,38], Michelson interferometer [20,39,40], etc.). Coherent-type sensors have the advantage of high measurement precision and can be widely applied in scenarios that require high precision.

This paper reviews the current research status of quantum sensing based on optical fibers. The structure of this paper is as follows: Section 1 highlights the importance of optical fiber quantum sensing for high-precision measurements. Section 2 presents the fundamental principles and experimental findings related to quantum light sources produced by optical fibers, along with several applications in optical fiber quantum sensing. Section 3 focuses on quantum sensing that employs optical fiber interferometers and its various applications. Lastly, Section 4 discusses future perspectives and opportunities for the advancement of quantum sensing using optical fibers.

2. Preparation and Application of Quantum States in Optical Fibers

In this section, we first summarize the quantum characteristics of quantum light fields and then introduce two methods for generating quantum light fields in optical fibers and

their basic principles, including the four-wave mixing optical parametric process based on third-order ($\chi^{(3)}$) nonlinearity and the Kerr effect. We also review the system and experimental progress of generating quantum light fields in optical fibers, including the generation of quantum-correlated beams and squeezed states.

2.1. Properties of Quantum States

Squeezed state—with the maturation of quantum optical states, researchers have discovered a non-classical quantum state (squeezed state) in which the fluctuation noise of a certain quadrature component is lower than that of the SNL. It has the following form:

$$\hat{S}(\zeta) = \exp[\frac{1}{2}(\zeta^* \hat{a}^2 - \zeta \hat{a}^{\dagger 2}), \tag{1}$$

where $\hat{a}$ and $\hat{a}^\dagger$ are the annihilation and creation operators of electromagnetic fields in quantum mechanics, respectively. $\zeta = re^{i\theta}$ is the squeeze parameter, r is the degree of squeeze, θ is the squeezed angle of the squeezing direction, and the squeezed operator $\hat{S}(\zeta)$ has the following properties:

$$\begin{aligned} \hat{S}^\dagger(\zeta)\hat{a}\hat{S}(\zeta) &= \hat{a}\cosh r - \hat{a}^\dagger e^{i\theta}\sinh r, \\ \hat{S}^\dagger(\zeta)\hat{a}^\dagger\hat{S}(\zeta) &= \hat{a}^\dagger\cosh r - \hat{a}e^{-i\theta}\sinh r. \end{aligned} \tag{2}$$

The annihilation operator $\hat{a}$ is a non-Hermitian operator that cannot be measured directly, but the annihilation operator of the states can be obtained by measuring its quadrature amplitude $\hat{X} = (\hat{a} + \hat{a}^\dagger)$ and quadrature phase $\hat{Y} = -i(\hat{a} - \hat{a}^\dagger)$. In particular, $\Delta\hat{X} = 1$ and $\Delta\hat{Y} = 1$ represent the vacuum state $|0\rangle$ and coherent state $|\alpha\rangle$, which are the least uncertain states. There is no doubt that the squeezed stated also satisfies the Heisenberg uncertainty relation $\Delta\hat{X}\Delta\hat{Y} \geqslant 1$. Interestingly, $\Delta\hat{X} < 1$ and $\Delta\hat{Y} > 1$ (the squeeze angle $\theta = 0$) is the quadrature amplitude squeezed state, while $\Delta\hat{X} > 1$ and $\Delta\hat{Y} < 1$ (the squeeze angle $\theta = \pi$) is the quadrature phase squeezed state. The phase space quadrature component fluctuation of quantum states is shown in Figure 1.

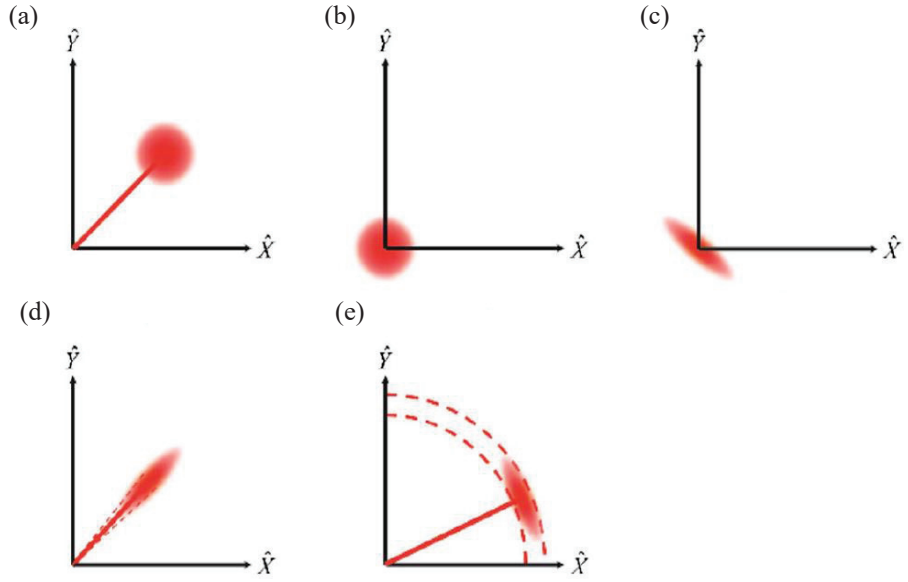

Figure 1. The phase-space distributions of the states. (**a**) Coherent state. (**b**) Vacuum state. (**c**) Vacuum-squeezedstate. (**d**) Quadrature phase squeezed state. (**e**) Quadrature amplitude squeezed state [41].

The form of the SNL makes it clear that the SNL can be reduced by increasing the intensity of the detection light field. This is one of the methods to improve measurement sensitivity in the classical field, such as the earliest Laser Interferometer Gravitation Wave

Observatory (LIGO) [10,11]. However, enhancing the light field's intensity also introduces additional radiation-pressure shot noise [42], which is a part of the standard quantum limit (SQL). Thus, the characteristic of squeezed state, where one of the quadrature components has less fluctuation than vacuum noise, enables the definite detection of signals that are lower than the SNL. This feature has absolute effectiveness in breaking through the SQL in quantum optics and is widely applied in quantum metrology [19,43], quantum sensing [44], and other fields [25,45–48]. Squeezed state fields can be generated through several methods, including the Kerr effect in optical fibers [49], polarization self-rotation in atomic ensembles [50], and optical parametric processes [51,52].

Entanglement state—when the output of a quantum system is a dual-mode light field, although both their quadrature amplitudes and phase fluctuations are greater than the SNL ($\Delta\hat{X}_{s,i} > 1$ and $\Delta\hat{Y}_{s,i} > 1$), the sum of their quadrature amplitudes or the difference between their quadrature phases is less than the SNL ($\left\langle(\Delta\hat{X}_s + \Delta\hat{X}_i)^2\right\rangle \to 0$, $\left\langle(\Delta\hat{Y}_s + \Delta\hat{Y}_i)^2\right\rangle \to \infty$; *or* $\left\langle(\Delta\hat{Y}_s - \Delta\hat{Y}_i)^2\right\rangle \to 0$, $\left\langle(\Delta\hat{X}_s - \Delta\hat{X}_i)^2\right\rangle \to \infty$). Such a dual-mode squeezed state is called a quantum entanglement state. The entanglement state can be directly generated by a nondegenerate parametric amplifier or obtained by the linear superposition of two single-mode squeezed states with the same frequency. O. Morin et al. experimentally achieved a mixed entanglement state of continuous variables and separated variables through type I and type II optical parametric oscillation cavitys [53]. T. Eberle et al. generated a continuous variable entanglement state by using the parametric down conversion of nonlinear crystals, and its inseparability was 10.45 dB lower than the SNL [54]. There is a strong correlation between entangled light fields, which can be widely applied in quantum teleportation [55], quantum sensing, and quantum precision measurement.

The intensity-difference squeezed state—when the fluctuation of the intensity difference between the two light fields generated by the quantum system is less than the SQL ($\left\langle(\Delta^2(\hat{I}_s - \hat{I}_i)\right\rangle < 1, \hat{I} = \hat{X}^2$), it is called the intensity-difference squeezing light field or twin beam. Nondegenerate optical parametric processes (including nondegenerate parametric down-conversion and four-wave mixing) are effective methods to generate intensity difference squeezed states [56,57]. Due to the quantum intensity correlation between the signal idler light in them, they can be effectively used for quantum imaging sensors [58] and other fields [59,60].

The polarized squeezed state—at least one Stokes component of a quantum system's output light field is lower than the quantum noise limit. The Stokes component of polarized squeezing light corresponds to the spin component of an atom and can be used as a quantum memory or quantum information processor [61]. F. Wolfgramm et al. utilized polarized squeezed light with a degree of 3.6 dB and improved the sensitivity of an optical magnetometer based on the Faraday effect by about 3.2 dB [62]. Professor J. M. Wang's research group conducted an experimental study on enhancing the SNR of spin-noise spectra using polarized squeezed light [63]. G. Leuchs's research group utilized the nonlinear Kerr effect of optical fibers and generated pulsed-polarized squeezed light through an asymmetric optical fiber Sagnac interferometer [49]. Furthermore, the Stokes operator is a conjugate variable that can be fully measured in direct detection (the measurement device is shown in Figure 2), and the measurement is relatively simple. It has significant application prospects in the construction of quantum networks [64,65].

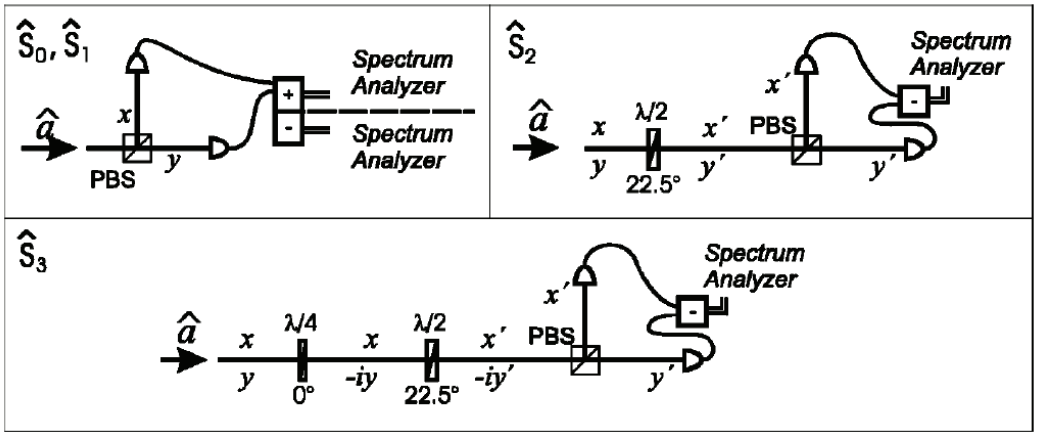

Figure 2. Measurement schemes for the Stokes operators' variances. Note: The sum of the intensities of the quadrature polarization components of the output light is the Stokes parameter $\hat{S}_0$. After passing through the polarization beam splitting prism, the difference in the intensities of the quadrature polarization components of the output light is the Stokes parameter $\hat{S}_1$ [49].

The polarized squeezing light field can be prepared by coupling the quadrature amplitude squeezed state and a strongly coherent light with polarization perpendicular to a polarized beam splitting prism; it has the following form:

$$\begin{aligned} \hat{S}_0 &= \hat{a}_x^\dagger \hat{a}_x + \hat{a}_y^\dagger \hat{a}_y, \\ \hat{S}_1 &= \hat{a}_x^\dagger \hat{a}_x - \hat{a}_y^\dagger \hat{a}_y, \\ \hat{S}_2 &= \hat{a}_x^\dagger \hat{a}_y + \hat{a}_y^\dagger \hat{a}_x, \\ \hat{S}_3 &= i(\hat{a}_y^\dagger \hat{a}_x - \hat{a}_x^\dagger \hat{a}_y), \end{aligned} \tag{3}$$

with the commutation relation of $[\hat{S}_0, \hat{S}_j] = 0$, $[\hat{S}_i, \hat{S}_j] = 2i\hat{S}_k$, $\{i, j, k\} = 1, 2, 3$. Non-zero means that these two operators cannot be measured simultaneously, and the uncertainty relationships of the variance of operator are $V_1 V_2 \geq \left|\langle \hat{S}_3 \rangle\right|^2$, $V_3 V_1 \geq \left|\langle \hat{S}_2 \rangle\right|^2$, $V_2 V_3 \geq \left|\langle \hat{S}_1 \rangle\right|^2$, where $V_j = \left\langle \hat{S}_j^2 \right\rangle - \langle \hat{S}_j \rangle^2$. One of the Stokes variances is not only lower than the coherence limit but also lower than their respective minimum uncertainty limits ($V_1 V_2 = \left|\langle \hat{S}_3 \rangle\right|^2$, $V_3 V_1 = \left|\langle \hat{S}_2 \rangle\right|^2$, $V_2 V_3 = \left|\langle \hat{S}_1 \rangle\right|^2$) [66]:

$$V_j < \langle \hat{S}_l \rangle < V_k, j \neq k \neq l. \tag{4}$$

When a linearly X-polarized quadrature amplitude squeezed beam ($\Delta \hat{X}_x < 1$, $\Delta \hat{Y}_x > 1$) overlaps with a linearly Y-polarized coherent beam with the same intensity ($\Delta \hat{X}_y = \Delta \hat{Y}_y = 1$),

$$\begin{aligned} \langle \hat{S}_0 \rangle &= 2\alpha^2, \langle \hat{S}_1 \rangle = 0, \langle \hat{S}_2 \rangle = 2\alpha^2, \langle \hat{S}_3 \rangle = 0; \\ \tilde{V}_1 \tilde{V}_2 &\geq 0, \tilde{V}_3 \tilde{V}_1 \geq 0, \tilde{V}_2 \tilde{V}_3 \geq 1, \end{aligned} \tag{5}$$

the normalized variance is

$$\begin{aligned} \tilde{V}_0 &= \tilde{V}_1 = \tilde{V}_2 = \frac{\Delta \hat{X}_x + 1}{2} < 1, \\ \tilde{V}_3 &= \frac{\Delta \hat{Y}_x + 1}{2} > 1, \end{aligned} \tag{6}$$

where $\tilde{V}_j = \frac{V_j}{\langle \hat{n} \rangle}$; in this situation $\hat{S}_0$, $\hat{S}_1$, and $\hat{S}_2$ are squeezed. $\hat{S}_1$ is conjugate to $\hat{S}_3$, and $\hat{S}_3$ is anti-squeezed.

When the polarized squeezing light field is prepared by coupling a linearly X-polarized quadrature amplitude squeezed beam ($\Delta\hat{X}_x < 1, \Delta\hat{Y}_x > 1$) with a linearly Y-polarized and equally intense quadrature amplitude squeezed beam ($\Delta\hat{X}_y < 1, \Delta\hat{Y}_y > 1$) on a polarized beam splitting prism,

$$\begin{aligned} \langle \hat{S}_0 \rangle &= 2\alpha^2, \langle \hat{S}_1 \rangle = 0, \langle \hat{S}_2 \rangle = 2\alpha^2, \langle \hat{S}_3 \rangle = 0; \\ \tilde{V}_0 &= \tilde{V}_1 = \tilde{V}_2 = \Delta\hat{X} < 1, \tilde{V}_3 = \Delta\hat{Y} > 1, \end{aligned} \tag{7}$$

in this situation, $\hat{S}_0$, $\hat{S}_1$, and $\hat{S}_2$ are squeezed to the same extent as a single amplitude squeezed beam to be ideal light sources in quantum information. Their more intuitive uncertainty is shown in Figure 3.

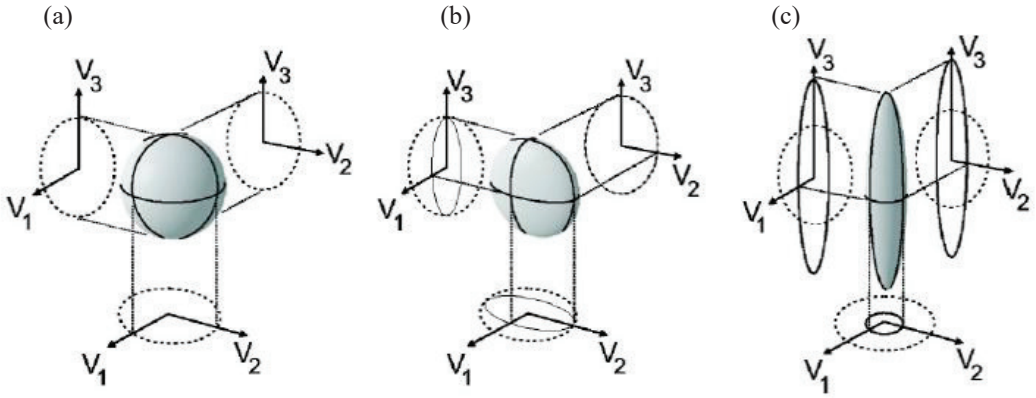

Figure 3. The variances of different polarization squeezed states. (**a**) Coherent states are represented by spherical uncertain volumes. (**b**) Coupling of quadrature amplitude squeezed state optical fields and vacuum states; only the squeezing below the coherence limit is observed, while no antisqueezing exists, indicating that no polarized squeezed light is generated. (**c**) By coupling the quadrature amplitude squeezed state light field with the coherent state or the quadrature amplitude squeezed state, respectively, the squeezing relative to the coherent beam can be observed [49].

In the above, we summarize the commonly used single-mode and multimode quantum states in optical fiber quantum sensing, revealing their reliability in achieving high-sensitivity single- and multi-parameter sensors. The introduction of the characteristics of different quantum states can help us deepen our understanding of the quantum light source generated by the fiber optic quantum sensing experimental system shown in the following content. Table 1 highlights the enhancements in the performance of the quantum sensing platform by certain quantum states.

Table 1. The performance metric of quantum sensing technology.

Years	Quantum Devices	Quantum States	The Measured Physical Quantity	The Improvement of SNR (SNRI) Compared to SNL
2010 [62]	OPO	the polarized squeezed state 3.6 dB	optical magnetometer	3.2 dB
2014 [67]	FWM in atomic ensemble	entanglement state	phase	4.1 dB
2015 [18]	FWM in atomic ensemble	entanglement state	micro-electro-mechanical-systems cantilever displacement	4 dB
2019 [20]	DOPO	squeezed state 7.2 dB	gravitational waves (LIGO)	3 dB

Table 1. *Cont.*

Years	Quantum Devices	Quantum States	The Measured Physical Quantity	The Improvement of SNR (SNRI) Compared to SNL
2020 [22]	FWM in atomic ensemble	entanglement state	atomic force microscope	3 dB
2020 [19]	DOPA	squeezed state 5.57 dB	phase	4.86 dB
2025 [68]	PA	dual pairs of entangled twin beams	distributed phase sensing	3 dB/advances the record of SNR so far achieved in photon-correlated interferometers by three orders of magnitude

2.2. Generation of Quantum States in Optical Fibers Based on Four-Wave Mixing Process

The optical parametric amplifier process based on the second-order nonlinear effect ($\chi^{(2)}$) of crystals is an effective device for generating squeezed states and entanglement states. Although the third-order nonlinear effect ($\chi^{(3)}$) on optical fibers is much weaker than the second-order nonlinear effect, the long nonlinear action length of optical fibers enables the four-wave mixing (FWM) process based on third-order nonlinearity to also generate quantum light sources such as entanglement states and intensity difference squeezed states. The fiber optic parametric amplifier (FOPA) amplifies the signal lights by utilizing the FWM in the optical fiber, and its structure is shown in Figure 4.

Injecting the strong pump light and the weak signal light together into the optical fiber gives the optical fiber as the nonlinear medium. When they satisfy the phase matching condition, the signal light will be amplified by the pump light and at the same time generate idler light that has a phase conjugate relationship with the signal light. The FWM process is prone to occurring in optical fibers and usually requires the pump light to be a single-frequency laser; then, the light field satisfies the energy conservation relationship ($2\omega_p = \omega_s + \omega_i$) and the momentum conservation relationship ($2k_p = k_s + k_i$). The input–output relationship of FOPA follows the Bogoliubov transformation [69]:

$$\hat{b}_{s,i} = G\hat{a}_{s,i} + g\hat{a}^{\dagger}_{i,s}, \tag{8}$$

where $G = \cosh(\chi^{(3)}|A_p|^2\tau), g = \sinh(\chi^{(3)}|A_p|^2\tau)$ and $|G|^2 - |g|^2 = 1$, $|A_p|^2$ is the intensity of pump light, $\tau = nL/c$ is the action time in the optical fiber, and L is the length of the optical fiber in FOPA.

When the injected light is the coherent state $|\alpha\rangle$ and the idler light is the vacuum state $|0\rangle$, the noise of the quadrature components of the output signal and the idler light of the FOPA is

$$\left\langle \Delta^2 \hat{X}_{s,i} \right\rangle = \left\langle \Delta^2 \hat{Y}_{s,i} \right\rangle = G^2 + g^2, \tag{9}$$

when the amplifier gain $G > 1$, the quadrature component noise is all higher than the SNL. However, due to the strong correlation between the output signal and idler light, the correlated noise can be removed in measurement by coherent addition or coherent subtraction. The normalized noise fluctuation of the quadrature amplitude difference and the quadrature phase sum between the two output fields are

$$\begin{aligned} \left\langle \Delta^2 \hat{X}_- \right\rangle &= \left\langle \Delta^2 (\hat{X}_s - \hat{X}_i) \right\rangle = (G-g)^2, \\ \left\langle \Delta^2 \hat{Y}_+ \right\rangle &= \left\langle \Delta^2 (\hat{Y}_s + \hat{Y}_i) \right\rangle = (G-g)^2, \end{aligned} \tag{10}$$

it is obvious that the output state of FOPA is an entanglement state light based on parametric processes, and the degree of entanglement can also be characterized by the degree of inseparability:

$$I_s = \frac{\langle \Delta^2 \hat{X}_- \rangle + \langle \Delta^2 \hat{Y}_+ \rangle}{2} = (G-g)^2 < 1, \tag{11}$$

it can quantitatively reflect the degree of quantum characteristics possessed by entanglement states.

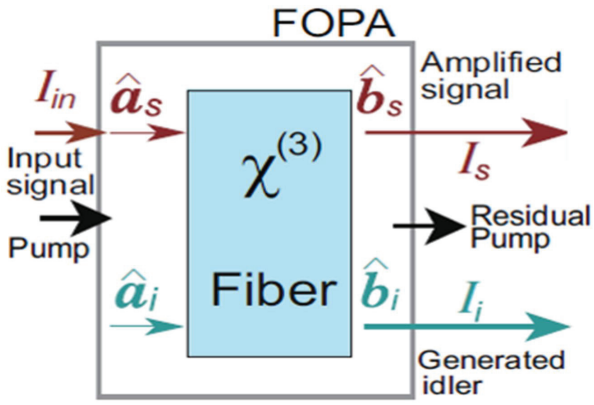

Figure 4. A typical diagram of the non-degenerate phase-insensitive FOPA. The pump light (Pump) and the weak signal light (Signal) are injected together into the optical fiber. The output of the optical fiber includes the amplified signal light (Amplified signal), the newly generated idler light (Generated idler), and the residual pump light (Residual pump) [70].

The normalized intensity noise of the output signal and idler light of FOPA are $R_s = R_i = G^2 + g^2$ [70]; the noise characteristics of FOPA are usually described by the noise figure (NF) $NF = 1 + \frac{g^2}{G^2}$. Combining the quantum operators of the differential current ($\hat{I}_t = \hat{b}_s^\dagger \hat{b}_s - r\hat{b}_i^\dagger \hat{b}_i$, r represents the ratio of the alternating current response during the detection process) in the correlation detection process of the two light fields (i.e., twin beams) generated by FOPA, the normalized intensity difference noise (i.e., the degree of intensity difference squeezed state) of the twin beams can be obtained as

$$\begin{aligned} R_t &= \frac{\Delta(I_t)^2}{I_s + r^2 I_i} \\ &= \frac{\Delta(I_s)^2 + r^2\Delta(I_i)^2 - 2rG^2g^2|\alpha|^2}{I_s + r^2 I_i} \\ &= \frac{1}{G^2+g^2}, (r=1) \end{aligned} \tag{12}$$

$$R_t = \frac{1}{(G+g)^2}, (r = r_{opt} = \frac{G}{g}), \tag{13}$$

where $\langle \hat{I}_{s,i} \rangle = \left\langle \hat{b}_{s,i}^\dagger \hat{b}_{s,i} \right\rangle$. Although the intensity noise of the signal light or idler light of FOPA is significantly higher than the SNL, the fluctuation of the intensity difference between the signal and the idler light generated by FOPA is lower than the SNL.

The twin beams generated by FOPA have the characteristic of intensity difference squeezing and the quadrature components of the generated signal and the idler light have entanglement characteristics. Optical fibers have the performance of lower loss in transmitting optical fields, which is conducive to the long-distance implementation of quantum technology. Therefore, it is of great practical significance to generate a quadrature amplitude entanglement state and intensity difference squeezed state in optical fiber systems [71–74]. As early as 1986, R. Shelby et al. generated quadrature amplitude squeezed

states with a squeezed degree of 0.6 dB by using the degenerate parametric amplifier process of optical fibers [75]. However, due to the influence of Raman noise and others, it was not until 2001 that J. Sharping et al. improved the squeezed degree of intensity difference squeezing generated by optical fibers to 1.1 dB [56]. Since then, researchers have devoted themselves to the generation and application research of quantum correlation light sources based on different optical fibers and have achieved good experimental results [76–80].

X. S. Guo et al. [57] demonstrated a compact and stable pulse intensity difference squeezed dual-beam based on an all-optical-fiber system. High-gain FOPA was achieved by pumping a 300 m long dispersion-shifted fiber (DSF) with a mode-locked fiber laser. The experimental setup is shown in Figure 5a. An optical fiber mode-locked laser (with a central wavelength of 1560 nm, a frequency bandwidth of 40 MHz, and a pulse width of approximately 150 fs) was used to generate both the signal and pump light through grating splitting to maintain coherence. A 90:10 fiber coupler was employed to couple 90% of the pump pulses (with a central wavelength of 1550 nm) and 10% of the signal pulses (with a central wavelength of 1570 nm) into the DSF, generating intensity difference squeezed light. The signal and idler lights were then coupled into free space via a fiber collimator and the degree of intensity difference squeezing of the generated twin pulse beams was assessed used a direct differential detection method. When the average power of the injected signal light was 1.2 mW and the average power of the pump light was 1.7 mW, the intensity difference squeezed degree was 2.6 dB at 3 MHz (as shown in Figure 5b). The effects of injection wavelength, pump bandwidth, and temperature on the twin pulse beams were discussed. After the gain optical fiber was cooled by liquid nitrogen, the temperature drop suppressed the noise caused by Raman scattering in the DSF. When the temperature of DSF was below 77 K, the injection power was 2 μW, and the gain g = 56, the system achieved the best intensity difference squeezed degree of 3.1 dB (as shown in Figure 5c). This advancement not only facilitates the implementation of quantum communication protocols within existing fiber networks but also has potential applications in high-precision measurement and sensing.

In addition, X. S. Guo et al. demonstrated an experiment of generating quadrature amplitude entangled light field at 1550 nm using a FOPA composed of two coarse wavelength division multiplexers (CWDMs) and a 300 m long DSF. The pump and the injected seed (with central wavelengths of 1552.5 nm and 1569 nm, respectively) were coupled into the DSF by CWDM1 [81]. The DSF served as the nonlinear medium to conduct the FWM process, generating signal and idler beams with entanglement. After separating the amplified signal and idler beams by CWDM2, the noise variances of the quadrature phase and quadrature amplitudes of the individual signal or idler beam were measured by homodyne detection systems (HDs/HDi) (as shown in Figure 6a). The noise variance of the difference and sum of the quadrature amplitudes between the pulse dual beams were approximately 1 and 0.8 dB below the SNL (as shown in Figure 6b, considering the efficiency, they were corrected to 4.2 and 3.6 dB, respectively). The obtained inseparability was $I = 1.63$ (as shown in Figure 6c), indicating that the generated entanglement state satisfied the Einstein–Podolsky–Rosen (EPR) criterion. This scheme has the potential to be developed into all-optical-fiber devices and is of great significance for practical applications in continuous variable quantum sensing.

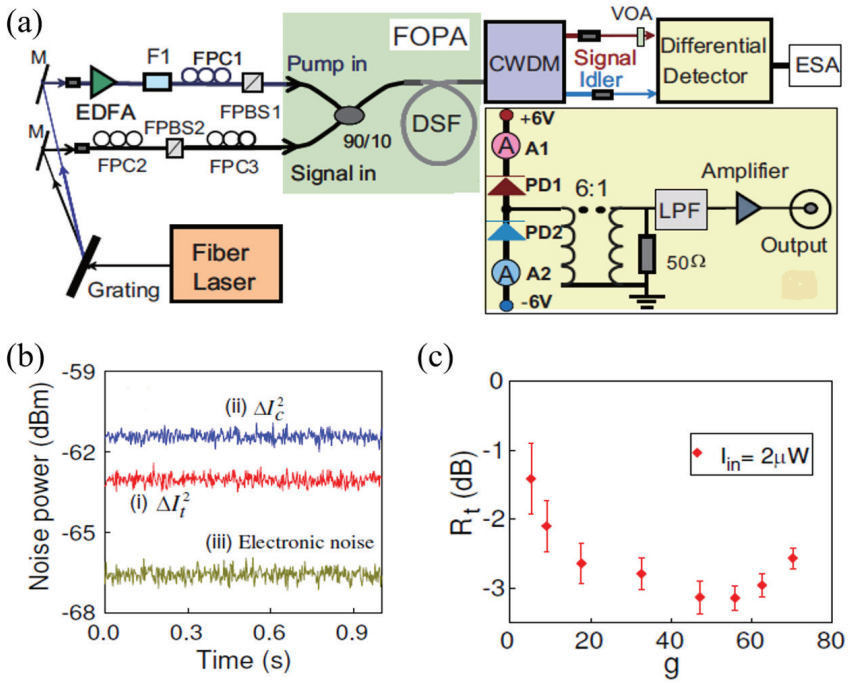

Figure 5. (**a**) The experimental configuration of a pulsed twin beam system using all-optical fiber. (**b**) (i) The noise level of the different photocurrents for the twin beams, (ii) SNL, (iii) electronic noise. (**c**) The noise reduction $R_t = I_t^2 / I_c^2$ in relation to gain g for an injection power 2 μW with the DSF at a temperature of 77 K [57].

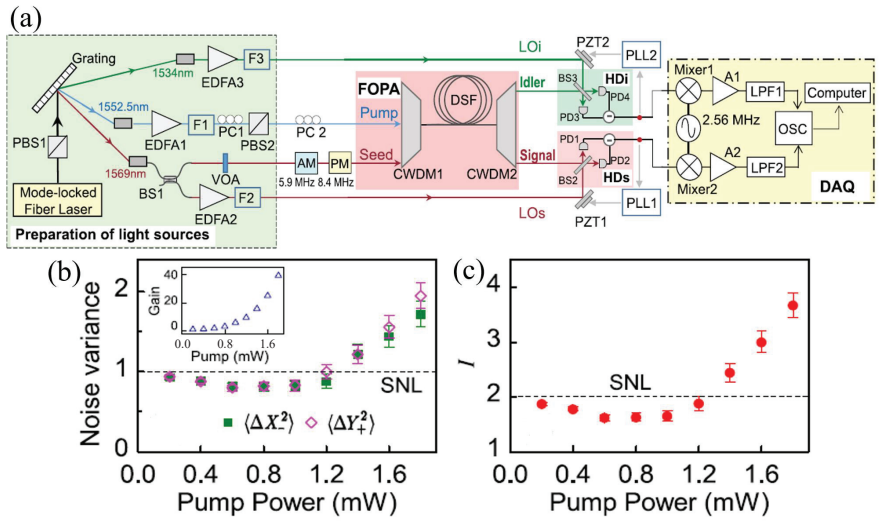

Figure 6. (**a**) The generation of continuous variable quantum entanglement. FOPA consisted of two CWDMs and a 300 m long DSF. (**b**) The variances $\Delta^2 \hat{X}_-$ and $\Delta^2 \hat{Y}_+$ were plotted as a function of the pump power, with the injected seed power set at approximately 2 nW. (**c**) The inseparability of twin beams was analyzed in relation to the average pump power [81].

It is obvious that the entangled degree of the entanglement states and the squeezed degree of the intensity difference squeezing generated by the above-mentioned FOPA have not reached a very high level, which is affected by Raman scattering and the lower detection efficiency of the measurement system. Y. H. Liu et al. focused on addressing these unfavorable factors in the FOPA system, optimized the dual-beam light source, further enhanced the intensity difference squeezed degree, and achieved a record intensity difference squeezed degree of 6.1 dB in the FOPA [82]. W. Zhao et al. achieved the time-domain measurement of the intensity difference squeezing of the two pulsed beams generated in

optical fibers through a fast-response differential detection system. The intensity difference squeezed degree of 3.8 dB (8.1 dB after correcting the detection loss) was measured in the time domain. This study provides support for the generation of multimode entanglement states in time-division multiplexing in optical fiber systems [83]. J. M. Li et al. used a high-gain phase-sensitive amplifier (PSA) to assist a balanced, pure difference detector in measuring the continuous variable entanglement state. They simultaneously coupled the two entangled fields produced by the pulse-pumped FOPA into the PSA and found that the normalized noise for both the difference and sum of the quadrature amplitudes of the two entangled fields was approximately 4.6 dB below the SNL [84]. In addition, quantum noise was usually coupled into the system by the internal degree of the amplifier during the amplifying process. Coupling the squeezed state or entanglement state with the internal degree could suppress the additional noise [85]. X. S. Guo et al. adopted the method of injecting the entangled beams generated by the FOPA into another FOPA. By making the input signal and idler light field in the second FOPA have quantum entangled characteristics, they could achieve destructive quantum interference, thereby reducing noise. The output noise of the signal and the idler light field was further reduced by 0.7 dB and 0.84 dB, respectively [86].

Many excellent achievements have been reported in quantum sensing experiments using entangled beams as sensing light. J. Kong et al. generated an entangled light through a parametric amplifier, in which one beam interacted with the physical quantity that affected the phase of light and then superimposed with another beam in a linear beam splitter, which was them eliminated through interference. The phase measurement sensitivity broke through the SNL [87]. C. Raphael et al. utilized the entangled light field generated by the FWM process of the rubidium atom gas as the sensing light source. This was combined with the micro-electro-mechanical-systems cantilevers (MEMSCs) to measure the displacement sensitivity of the MEMSCs. The displacement of the MEMSCs beyond the SNL was 4 dB, achieving a quantum MEMSC sensor [18]. R. C. Pooser et al. also used the entangled light generated by the FWM process of the rubidium atom gas as the sensing light to measure the displacement of an atomic force microscope microcantilever, achieving the first practical application of nonlinear interferometry. The quantum noise was lower than the SNL by about 3 dB, corresponding to the displacement of the quantum, enhanced by about 1.7 fm/$\sqrt{\text{Hz}}$ [22]. These studies were all based on atomic ensemble or second-order nonlinear parametric processes to achieve quantum sensing. There are also reports on optical fiber quantum sensing that generates entangled light based on FOPA systems.

H. L. Wang et al. [88] conducted experiments to showcase a quantum-enhanced tapered optical fiber sensor that utilized intensity difference squeezed light along with a traditional tapered optical fiber design (as shown in Figure 7a). A sensing beam, derived from a pulsed dual-beam generated by a FOPA, was coupled into the tapered optical fiber sensor, which was formed by connecting two tapers to a single-mode optical fiber. This sensing beam was then measured in conjunction with a reference beam that passed through a variable optical attenuator (VOA). The curvature and temperature were measured simultaneously. Since the pulsed dual-beam was intensity difference squeezed light, it effectively improved the SNR and sensitivity of the tapered optical fiber sensor. The VOA was introduced into the reference beam to achieve two kinds of measurements: one was a balanced measurement where the intensity of the sensing and the reference beams were exactly equal and the other was an unbalanced measurement where the intensity of the sensing and the reference beams were different. The squeezed degree of intensity difference squeezed light generated by the FOPA was 2.9 dB (as shown in Figure 7b). The SNR of curvature sensing was maximally improved by about 1.10 dB under balanced measurement conditions and 0.98 dB under unbalanced measurement conditions. The

SNR of temperature sensing was maximally improved by about 1.14 dB under balanced measurement conditions and about 0.64 dB under unbalanced measurement conditions (as shown in Figure 8). This quantum-enhanced tapered optical fiber sensor demonstrates greater sensitivity and has potential applications in surface plasmon resonance sensing and humidity detection.

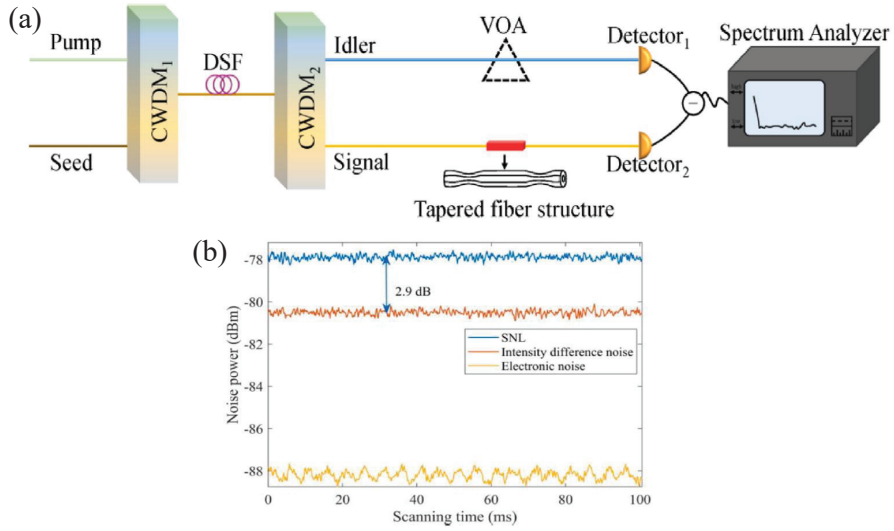

Figure 7. (**a**) Experimental setup. The light source was a femtosecond laser (with an average power of 104 mW, pulse width of 65 fs, and repetition frequency of 50 MHz). FOPA consisted of two CWDMs and one DSF. The lengths of the first and second tapers in the tapered fiber structure were 300 µm and 400 µm, respectively, with a distance of 1.2 cm between the two tapers. (**b**) The noise power of the intensity difference [88].

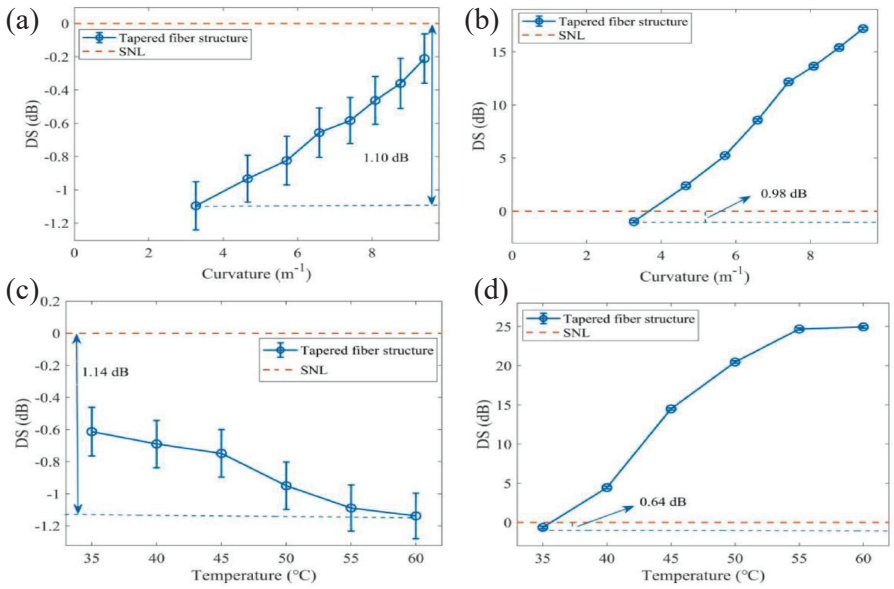

Figure 8. The relationship between the degree of intensity difference squeezing (DS) and curvature examined under (**a**) balanced detection conditions and (**b**) unbalanced detection conditions. Additionally, the dependence of DS on temperature was analyzed under (**c**) balanced detection conditions and (**d**) unbalanced detection conditions. The balanced detection condition occurred when the reference beam was reduced to the same intensity as the sensing beam; if not, it was referred to as the unbalanced detection condition. In balanced detection conditions, the two beams could more effectively eliminate quantum noise, resulting in improved sensitivity [88].

2.3. Generation of Quantum States in Optical Fibers Based on Kerr Effect

The Kerr effect based on the third-order nonlinearity of optical fibers causes the refractive index of the material to change with the variation of optical power when light propagates in the material:

$$n = n_0 + n_2 I \tag{14}$$

where n the refractive index in optical fibers and I is the intensity of light.

As different amplitudes undergo different rotations in the phase space, the phase of the light field is modulated, the noise between the quadrature components of the light is reduced, and the coherent state is converted to the squeezed state (as shown in Figure 9). Researchers have also paid considerable attention to theoretical and experimental research on generating quantum states based on the Kerr effect in optical fibers [28,89–94].

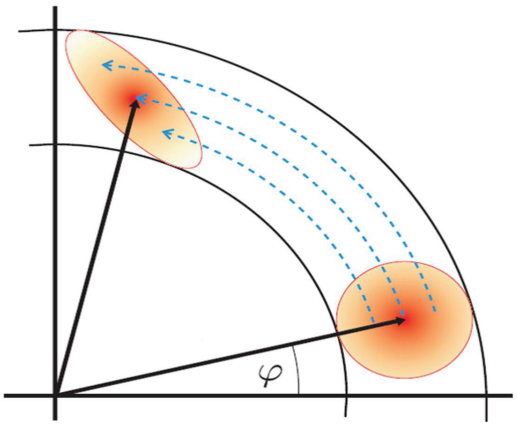

Figure 9. Schematic representation of the effect of a Kerr medium on a single mode in the phase space. φ is the polar angle in phase space [95].

R. F. Dong et al. [96] conducted an experiment to generate a polarized squeezed state using ultrasort photonic pulses passing through a birefringent fiber in a single pass (as shown in Figure 10). Ultrashort pulses with the same optical power were coupled into two quadrature polarization axes x and y of a 13.2 m long polarization-maintaining (PM) fiber (with a nonlinear refractive index of $n_2 = 2.9 \times 10^{-20}$ m^2/W). Due to the Kerr effect of optical fiber, two independent Kerr squeezed beams were obtained at the output end of the optical fiber. Birefringence compensators were utilized to give them a relative phase shift of $\frac{\pi}{2}$. Stokes measurements were carried out using a half-wave plate $\frac{\lambda}{2}$ and a polarization beam splitter. Theoretical analysis revealed that if $\Delta^2 \hat{S}_\theta < \left|\langle \hat{S}_3 \rangle\right| = \alpha^2$, a polarized squeezed state was generated. $\Delta^2 \hat{S}_\theta = \alpha^2 \Delta^2 \hat{X}_\theta$ indicated that the noise of the Stokes parameter $\hat{S}_\theta$ was connected to the noise of the Kerr squeezed mode at the same angle, and the noise statistics of the optical fiber squeezed state could be directly described by measuring the polarized squeezed state. The experiment measured the maximum squeezed degree observed at an energy of 98.6 pJ, which was 6.8 dB. Meanwhile, experimental evidenced that depolarizing guided acoustic wave Brillouin scattering (GAWBS) led to a decrease in squeezing at lower pulse energies. Beyond the soliton energy of approximately 120 pJ, the decline in squeezing was attributed to Raman effects. Furthermore, the measurement system did not require local light. Quantum noise detection could be achieved by directly measuring the output light of the optical fiber. Besides reducing detection loss, it was also conducive to improving the stability of the measurement system and reducing the measurement difficulty, which can further enhance the sensitivity of quantum sensing.

In the above-mentioned practical measurements, the quantum states generated by the Kerr effect in the optical fiber had lower noise than those generated by the FWM in the optical fiber. Employing optimized photodiodes with all-fiber architectures suppresses signal attenuation to improve squeezing levels; the precision trimming of waveguide length may further improve quantum state squeezed degree.

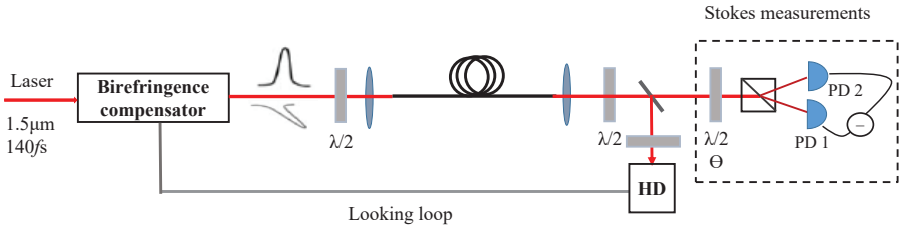

Figure 10. Experimentalsetup for efficient polarization squeeze generation. The central wavelength of the pulsed light was 1.5 μm with a bandwidth of 19 nm (pulse width of 140 fs, repetition frequency of 163 MHz). The squeezed angle is θsq (the rotation angle of squeezed quadrature relative to amplitude quadrature).

The loss during the quantum state transmission process will greatly reduce its noise suppression degree. When generating quantum states by the optical parameter amplification process and the Kerr effect in optical fibers, the loss of the optical fiber system is lower. Compared with the method generated by second-order nonlinear crystals, it has the advantage of being easier to couple into optical fibers, which also minimizes loss during the transmission process. F. Kaiser et al. [97] conducted the first squeezing experiment entirely based on optical fiber components at a telecom wavelength, achieving the collection and transmission of the squeezed light using only telecom fiber components. On the one hand, this provided a more compact and stable nonlinear optical device. On the other hand, there was no need for the calibration work of spatial pattern matching, with direct modification possible by connecting additional optical fiber components. This paved the way for universal experiments of continuous variable quantum sensing. If optical fiber nonlinear technology can replace the waveguide nonlinear technology in this scheme, a practical, all-optical-fiber quantum sensing system may be achieved [97,98].

3. Optical Fiber Quantum Interferometer in Quantum Sensing

Optical interferometers or the interference effects of light are effective and widely used measurement methods in the field of optics. A number of studies have proved that interferometers have high measurement precision that is difficult to surpass through direct detection. With the maturation of quantum technology, interferometers tend to construct high-precision structures and optimize anti-loss mechanisms. This section reviews the relevant research on all-optical-fiber nonlinear interferometers, optical fiber Sagnac interferometers, and optical fiber Mach–Zehnder interferometers in quantum sensing. There are mainly two methods for quantum sensing based on optical fiber interferometers: one is combining the quantum source generated by the nonlinear process in the optical fiber with the optical fiber interferometer to achieve material measurement; the other is combining the quantum source generated by other nonlinear processes with the optical fiber interferometer. Both of these two methods are covered in this section.

3.1. The All-Optical-Fiber Nonlinear Interferometer

The phase difference between the two beams in an interferometer is highly sensitive to the changes in physical quantities that affect the two interference paths. Therefore, high-precision quantum sensing measurements have been achieved for biological tissue [99], displacement [18,22,100], phase [101], and angular rotation measurement [102]. With the

increasingly high demand for sensing precision, researchers not only use quantum light fields as sensing light beams but also continuously design and optimize the structure of interferometers to achieve higher sensitivity and precision [17,19,67,103], further expanding the application scope of quantum sensing.

The nonlinear interferometer was proposed by Yurke et al. [104] in which the nonlinear beam splitter is used to replace the linear beam splitter of the traditional interferometer. The entanglement state light is generated by the first nonlinear beam splitter (NBS1). By applying the entangled signal and idler light as the sensing light, the signal of the measured object (the signal generated by the phase or amplitude modulation of the light during the interaction process between the measured object and the light field) can be loaded onto the entangled beam. Then, the two beams of light carrying the measured signal are simultaneously input into the second nonlinear beam splitter (NBS2). There is quantum entanglement between the signal and the idler light output by NBS1, when the two light beams interfere in NBS2, the correlated noise is coherently eliminated, reducing the output noise and achieving quantum-enhanced precision measurement. Processes such as parametric down conversion and FWM can be used as a nonlinear beam splitters. The gain characteristics of nonlinear parametric processes are affected by the phase relationship between the two levels of NBS and exhibit nonlinear interference effects; thus, this device is called a nonlinear interferometer. In recent years, there have been many quantum enhanced sensing experiments based on nonlinear interferometers [67,105,106]. Y. H. Liu et al. [107] also utilized a nonlinear interferometer based on the FWM process in FOPA to achieve multi-parameter measurement and joint measurement beyond SNL. Taking the nonlinear interferometer based on OPA as an example (as shown in Figure 11), introducing the basic principle of its measurement precision can help us deepen our understanding of the measurement performance and anti-loss characteristics of this nonlinear interferometer (NLI).

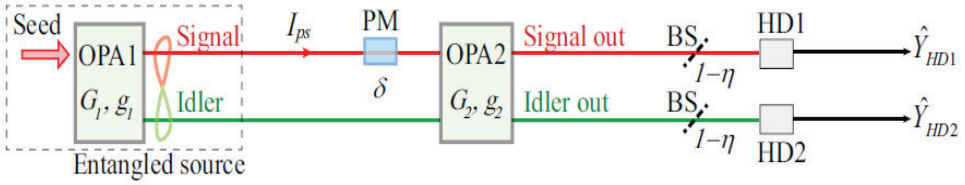

Figure 11. Phase measurement schemes by OPA-based NLI. BS, beam splitter with transmission efficiency of $1-\eta$ was used to model non-ideal detection efficiency; HD_{1-2}, homodyne detection [107].

When applying homodyne detection (HD) to measure phase sensing, the measured quantities are the signal and noise power of the quadrature amplitude (phase) of the output state. The noise fluctuation of the quadrature phase of NLI's output states are ($\Phi = \pi$)

$$\begin{aligned} \left\langle \Delta^2 \hat{Y}_{HD1} \right\rangle &= \left\langle \hat{Y}_{HD1}^2 \right\rangle - \left\langle \hat{Y}_{HD1} \right\rangle^2 \\ &= (G_1 G_2 - g_1 g_2)^2 + (g_1 G_2 - G_1 g_2)^2, \end{aligned} \tag{15}$$

contracting to Equation (9), we find that the noise suppression ratio of NLI is

$$\begin{aligned} R_{NLI} &= \frac{(G_1 G_2 - g_1 g_2)^2 + (g_1 G_2 - G_1 g_2)^2}{(G_2 + g_2)^2} \\ &\approx (G_1 - g_1)^2 < 1, \end{aligned} \tag{16}$$

the nonlinear interferometers can achieve noise suppression, and the SNR is

$$SNR_{HD1} \approx \frac{2I_{ps}\delta^2}{(G_1 - g_1)^2} = 2(G_1 + g_1)^2 I_{ps}\delta^2. \tag{17}$$

The SNR surpasses its in traditional interferometer. When only OPA2 is used for phase measurement ($G_1 = 1, g_1 = 0$), the SNR is

$$SNR \approx \frac{4\eta G_2^2 I_{ps}\delta^2}{\eta(G_2^2 + g_2^2) + 1 - \eta} \approx 2I_{ps}\delta^2, (G_2 \gg 1) \tag{18}$$

it is certain that adding an amplifier prior to beam splitting will not affect the SNR of the output signal; however, it can render the output signal less susceptible to detection loss. As a result, NLI can attain precision measurements that surpass SNL and possesses the ability to withstand losses from external detection.

Y. H. Liu et al. [108] utilized two FOPAs based on the FWM as the nonlinear beam splitters to constructe a nonlinear interferometer and achieve a scheme for the simultaneous high-precision measurement of quadrature amplitudes and quadrature phases and the joint measurement of multiple non-commutation physical quantities in light fields. All the sensitivities of them were beyond the SNL (as shown in Figure 12a). Each FOPA consisted of a 300 m long DSF and two CWDMs, which were used to separate and combine fields. The signal beam from the output of FOPA1 passed through the amplitude modulator (AM) and the phase modulator (PM) in sequence, encoding the information onto two or more quadrature amplitudes. The encoded signal beam and idler beam were amplified by FOPA2 and output the signal and idler light from the output ports. When measuring the two parameters of quadrature amplitude $\hat{X}_s(0)$ (with $SNR_{nl} = 2(G_1 + g_1)^2 I_{ps}\epsilon^2$) and quadrature phase $\hat{X}_i(\frac{\pi}{2})$ (with $SNR_{nl} = 2(G_1 + g_1)^2 I_{ps}\delta^2$), the signal and idler output of the interferometer were detected by HD1 and HD2, respectively. The SNR of the signal of the measured object on the two quadrature components was simultaneously improved by approximately 20% (as shown in Figure 12b). When jointly measuring the signals on any quadrature components (ϵ and $\xi(\pi/4)$), HD1 still measured the quadrature amplitude components while locking the measurement object at $\hat{X}_s(\frac{\pi}{4})$ of HD2. The modulated signal $\xi(\pi/4)$ still showed an approximately 20% improvement of SNR at 1 MHz (as shown in Figure 12c). This scheme also achieved a joint measurement of the three parameters ϵ, δ, and $\xi(\pi/4)$ by HD1, HD2, and HD3, respectively, with their noise levels lower than the SNL by about 20%. The scheme of multi-parameter joint measurement using NLI could be extended to jointly measure multiple (>2) quadrature components at any angle. This experiment made use of AM and PM to simulate the measured quantity; it also had the advantage of being able to mix different types of waves [109–112] and objects with signal beams to achieve practical measurement. It has broader significance and application potential for the sensing of various physical observation quantities.

Y. H. Liu et al. [107] also employed two FOPAs, which operated based on the FWM process, as nonlinear beam splitters to create a nonlinear interferometer for dual-beam sensing (as shown in Figure 13a). The signal and idler light produced by FOPA1 were loaded onto a phase modulation signal (with a frequency of 1.56 MHz and a modulation depth of δ) together by PM and then amplified by FOPA2. The outputs of the signal and idler light from the interferometer were detected by HD1 and HD2, respectively, when they were locked in the quadrature phase components. The results were then processed by the joint measurement system, yielding an output signal of $\hat{Y}_{JM} = \hat{Y}_{HD1} + \hat{Y}_{HD2}$. Compared to a traditional interferometer, this joint measurement approach enhanced the SNR of phase measurement by approximately 3.9 dB (as shown in Figure 13b,c). The SNR of

the joint measurement scheme surpassed that of the direct measurements from HD1 and HD2 because it could extract subtle information that was hidden within the correlation characteristics of the signal and idler light.

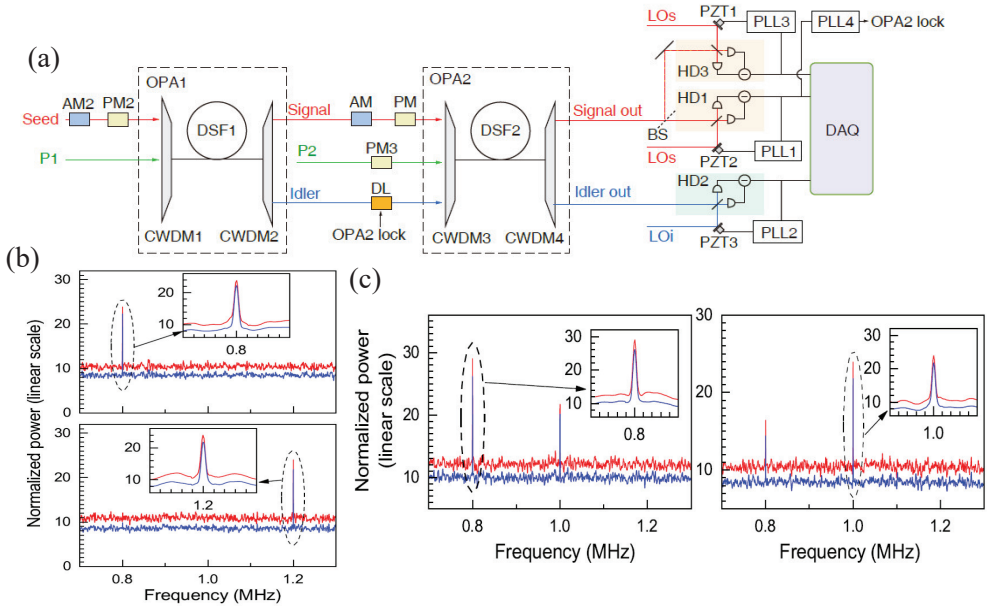

Figure 12. (**a**) Experimental setup of NLI-based FOPA. (**b**) Joint measurement results: the blue traces were achieved by NLI when the input power $I_{in} = 1$ nW, the intensity of probe $I_{ps} = 2$ nW, and the power gains were $G_1^2 = 2, G_2^2 = 9$. In contrast, the red traces were derived from a classical scheme with $P1 = 0$ (namely, $G1 = 0$ and $I_{in} = 2$ nW, $G_2^2 = 9$). The peaks observed at 0.8 and 1.2 MHz corresponded to the modulation signal power ϵ (measured by HD1) and δ (measured by HD2), respectively. (**c**) The joint measurement results for the encoded non-orthogonal quadrature phase amplitudes $\hat{X}_s(0)$ (at 0.8 MHz) measured by HD1 and $\hat{X}_s(\frac{\pi}{4})$ (at 1.0 MHz) measured by HD2 [108].

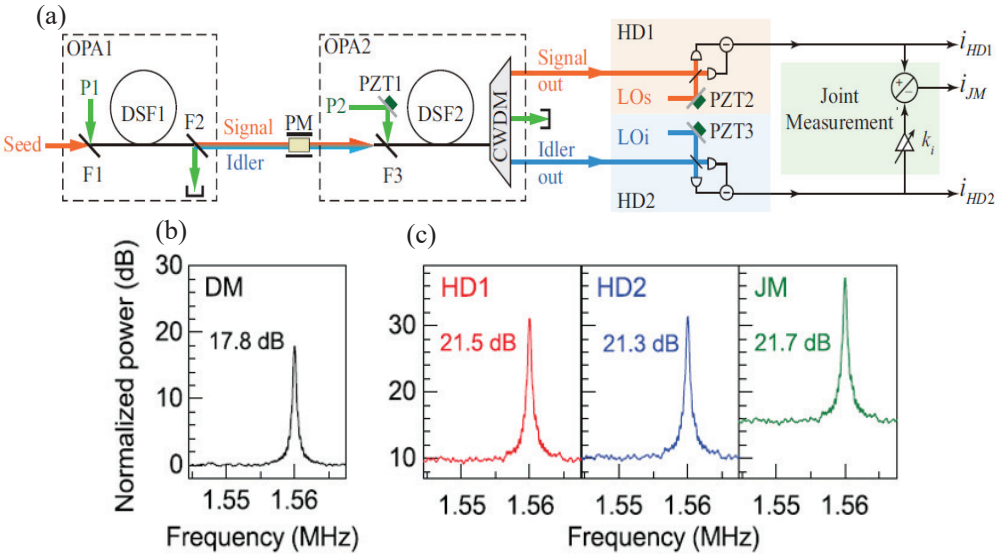

Figure 13. (**a**) Experimental setup of a dual-beam nonlinear interferometer based on FOPA. (**b**) The power spectrum of the output signal measured by HD1 when $Ips = 200$ pW and $G_1 = G_2 = 1$, $g_1 = g_2 = 0$ (namely, traditional interferometer). (**c**) The power spectrum of the output signal of NIL measured by HD1, HD2, and joint measurement (JM) when $Ips = 200$ pW, $G_1^2 = 2.5, G_2^2 = 12$ [107].

3.2. The Optical Fiber Sagnac Interferometer

The optical fiber Sagnac interferometer is widely recognized for its capability to measure rotation in gyroscopes [113–115]. It has been extensively utilized across various

fields for a considerable time. The asymmetric optical fiber Sagnac interferometer is able to achieve optical soliton squeezing [90,116]. Additionally, it has numerous applications, including in temperature sensing [117,118], force sensing for weighing small objects [119], strain sensing [120], biochemical sensing [121], and twist sensing [122], among others [123].

The Sagnac interferometer operates on the principle of the Sagnac effect. When two light waves propagate towards each other in a closed optical loop, the rotation of the loop and other factors will cause the lengths of the propagation paths of the two light waves to be different. This results in a phase difference, creating alternating bright and dark interference fringes. Typically, optical fiber Sagnac interferometers are constructed by connecting high birefringence fibers in a closed loop. This setup causes the effective refractive indices for the two polarization directions (the fast axis and slow axis or X-axis and Y-axis) to differ, resulting in a phase difference between the two polarization modes:

$$\Phi = 2\pi BL/\lambda \tag{19}$$

where $B = n_x - n_y$ is phase birefringence as a function of wavelength and temperature; L is the length of the high birefringence optical fiber. As external physical conditions (like temperature and stress) change, the phase difference of the transmitted light will also vary, leading to the deviation of the interference wavelength, and a change in the output transmission intensity. Consequently, by monitoring the movement of the central wavelength of the transmission spectrum and the output transmission intensity, one can assess changes in external environmental parameters.

Compared with the traditional optical fiber Sagnac interferometer, the quantum optical fiber Sagnac interferometer has higher sensitivity and a wider application space because it can make the noise of the sensing beam lower than that of the SNL. M. Mehmet et al. [124] injected a squeezed optical field with a squeezed degree of 6.4 dB into the idler port of an optical fiber Sagnac interferometer. The mode matching of each part of the system caused a total loss of 5%. Their system achieve a quantum-enhanced optical fiber Sagnac interferometer with a 4.5 dB improvement in the SNR of the 10 m long Sagnac interferometer. Compared with the 14% optical loss in the quantum-enhanced spatial Sagnac interferometer in Ref. [36], the quantum-enhanced optical fiber Sagnac interferometer takes advantage of the lower loss of optical fibers and has the potential to solve the problem of loss severely reducing the quantum properties of quantum states. J. Xin et al. [125] constructed a novel, nonlinear Sagnac interferometer by substituting the beam splitter in the conventional Sagnac interferometer with FWM technology. This new design exhibits improved sensitivity to angular velocity compared to the traditional Sagnac interferometer. M. Fink et al. [126] injected the two-photon N00N state into an optical fiber Sagnac interferometer, achieving a quantum-enhanced measurement of the phase shift caused by rotational motion. Although this sensor does not yet have a competitive edge over commercial gyroscopes, it has been proven that quantum enhancement is an important step towards achieving the ultimate measurement sensitivity of optical fiber gyroscopes.

The above are experiments on achieving optical fiber quantum sensing based on quantum state injection into a Sagnac interferometer. H. L. Wang et al. [127] proposed the method of combining an all-optical-fiber, dual-mode, squeezed state with a Sagnac interferometer, achieving quantum enhancement experiments on the sensitivity of strain and curvature sensors (as shown in Figure 14a). This experiment utilized FOPA to generate a dual-mode squeezed state. The signal beam output by FOPA was injected into the optical fiber Sagnac interferometer as the sensing beam. The idler beam output by FOPA was used as the reference beam and passed through a VOA to maintain the same intensity as the sensing beam to achieve balanced measurement. Then, they were injected into the HD system together to measure the intensity difference noise between them. The optical

fiber Sagnac interferometer was fabricated by splicing polarization-maintaining fibers between single-mode fibers. The squeezed degree of the intensity difference squeezed state generated by FOPA was 2.9 dB (as shown in Figure 14b). The SNR of strain sensing was quantum-enhanced by a maximal factor of 1.54 dB under balanced measurement conditions and 1.39 dB under unbalanced measurement conditions (as shown in Figure 15a,b). The SNR of curvature sensing is quantum-enhanced by a maximal factor of 1.31 dB under balanced measurement conditions and 1.36 dB under unbalanced measurement conditions (as shown in Figure 15c,d). This all-optical-fiber quantum Sagnac interferometer can be easily extended to the sensing of other physical parameters (such as temperature, refractive index, force, and so on) and will realize many applications that require precise sub-Poisson measurements.

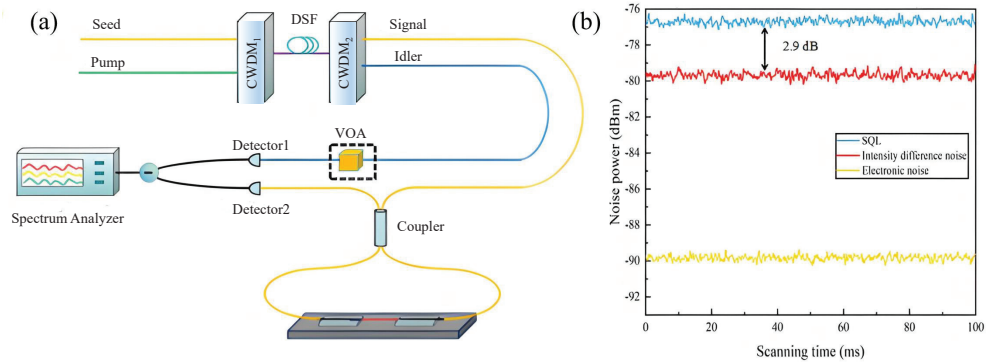

Figure 14. (**a**) Experimental setup of all-optical-fiber Sagnac interferometer used to perform quantum enhanced strain and curvature sensing. FOPA consisted of two CWDMs and a DSF. (**b**) The intensity difference noise power [127].

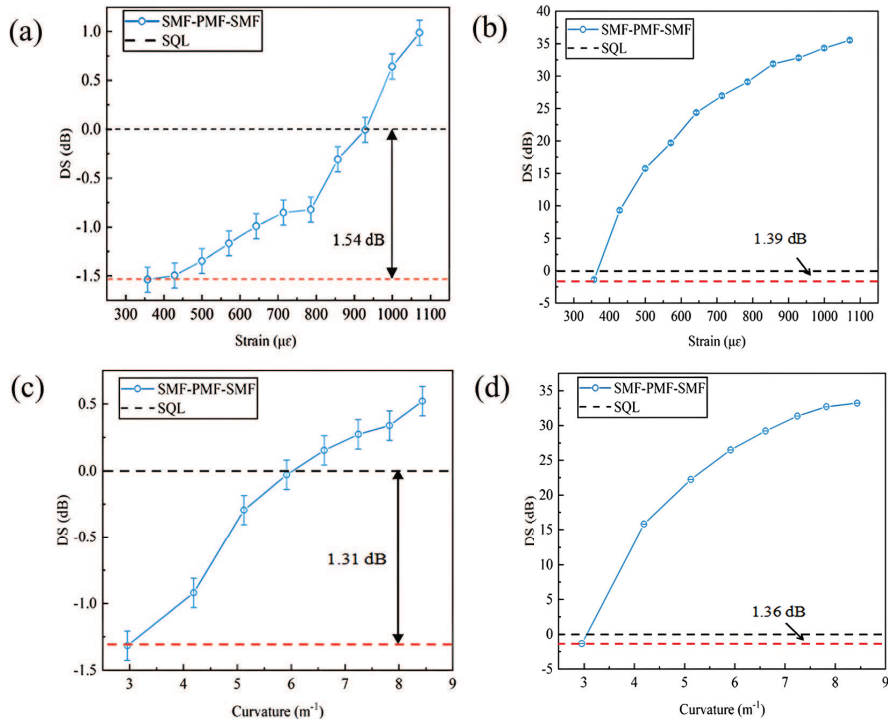

Figure 15. The dependence of DS under (**a**) balanced detection conditions and (**b**) unbalanced detection conditions on strain and under (**c**) balanced detection conditions and (**d**) unbalanced detection conditions on curvature. The red dotted line represents the experimental results. The balanced detection method achieved better quantum-enhanced results in a wide range [127].

3.3. The Optical Fiber Mach–Zehnder Interferometer

There are primarily two kinds of optical fiber Mach–Zehnder interferometers (MZI). One is the traditional MZI (as shown in Figure 16a), which applies two couplers to split and combine the light beam. After the coupler splits the light into two beams, they travel through two optical fibers over equal distances (referred to as the sensing arm and the reference arm) before being recombined. When external factors affect the sensing arm, they alter the phase difference between the two arms, resulting in changes to the intensity or wavelength of the interference light. By measuring the light intensity at the output port or the central wavelength, one can determine variations in the external parameters. Another type is the in-line MZI [128,129], which integrates the coupler and two arms of the traditional MZI into a single optical fiber. This compact design streamlines the sensor's structure and enhances stability. Notably, the in-line MZI sensor featuring a single mode–multimode–single mode (SMS) configuration, which consists of a multimode optical fiber spliced between two single-mode fibers, has garnered significant interest since its straightforward manufacturing process [34,130–132]. This sensing design combines two distinct types of optical fibers. In multimode optical fibers, various cladding modes are excited to interfere with the core mode, but it is primarily the interference between the core mode and the dominant cladding mode that plays a crucial role in the interference effect. The phase difference between these two modes is

$$\Phi = 2\pi(n_{co} - n_{cl})L/\lambda \tag{20}$$

where n_{co} and n_{cl} are the effective refractive indices of the two modes, respectively, λ is wavelength of light, and L represents interference length in the sensing structure. The wavelength dip of the interference at the minimum light intensity is

$$\lambda_m = 2\pi(n_{co} - n_{cl})L/(2k+1). \tag{21}$$

In sensing, the measurement of external factors can be accomplished by tracking the variation of the wavelength dip.

The interference between the core mode and the cladding mode is a mainstream interferometer mode of the in-line MZI. Besides the SMS structure, the fused biconical taper method in a single-mode fiber (SMF) can also facilitate this interference. Z. Tian et al. [133] conducted a comprehensive study on a fiber refractive index sensor utilizing the tapered fiber structure in an in-line MZI. P. Lu et al. [134] developed an in-line MZI by connecting two tapered fiber structures in series and evaluated its capabilities for sensing temperature and refractive index. They successfully measured both temperature and refractive index simultaneously (as shown in Figure 16b). Wang et al. [135] introduced an MZI refractive index sensor that employs a double tapered design. Two SMFs were tapered and fused together to create a tapered structure. The sensor demonstrated a sensitivity of 158.4 nm/RIU within a refractive index range of 1.33–1.3792.

F. Liu et al. [136] injected the squeezing light field into the optical fiber MZI to achieve quantum-enhanced optical fiber sensing based on the optical fiber MZI (as shown in Figure 17a,b). The squeezed vacuum state generated by NOPA was coupled into one port of the optical fiber MZI for quantum detection. The other port received local light, which was modulated in amplitude at megahertz frequencies to avoid low-frequency noise. The resulting interference signal was then analyzed using balanced homodyne detection (BHD), achieving a 2 dB reduction in phase noise below the SNR at frequencies in the tens of kHz range (as shown in Figure 17c). This approach incorporates quantum resources into the optical fiber MZI, showing promising applications for the high-precision sensing of temperature, strain, and other parameters. Similarly, G. H. Kang et al. [137] utilized the

same technique to achieve a 3 dB quantum enhancement in phase modulation measured by the quantum-enhanced optical fiber MZI within the frequency range of 40 kHz to 200 kHz.

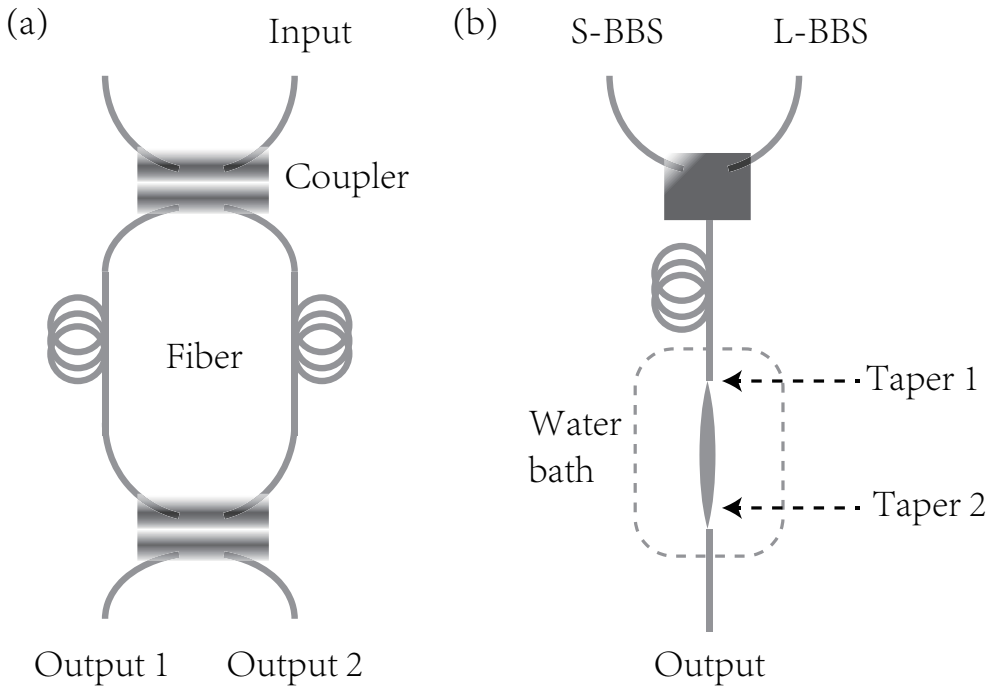

Figure 16. (**a**) Schematics of traditional fiber MZI. (**b**) The tapered fiber and two tapered fibers formed an in-line MZI.

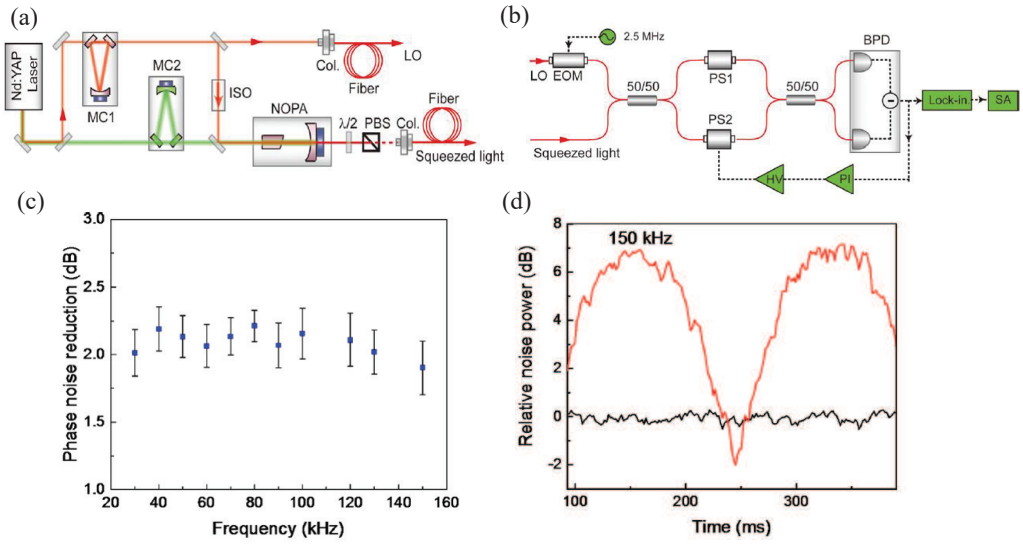

Figure 17. (**a**) Experimental setup of the generation of squeezed vacuum states. (**b**) Experimental setup for squeezed states input optical fiber MZI. (**c**) The phase noise of quantum-enhanced optical fiber MZI from 30 kHz to 150 kHz. (**d**) The noise spectra of the quantum-enhanced optical fiber MZI output at 150 kHz [136].

At present, there are not a large number of quantum-enhanced sensing experiments based on in-line optical fiber MZI. If quantum technology can be successfully combined with an in-line optical fiber MZI to achieve quantum optical fiber sensing, this will simplify the experimental structure while achieving the highly sensitive sensing of more physical quantities. These results from the optical fiber interferometer open the door to real-world quantum sensing based on quantum technology [97,98].

4. Summary and Outlook

In this review, we explored the key principles of quantum state manipulation in optical fiber systems, which form the basis of quantum-enhanced sensing protocols. Quantum sensing applications based on optical fiber quantum states and optical fiber interferometers were discussed and the potential application of optical fiber systems for quantum sensing was explored. In conclusion, whether it is the generation of quantum states based on the third-order nonlinear effects in optical fibers or the combination of quantum states generated by other processes (such as second-order nonlinear processes and atomic ensemble FWM processes) with optical fiber sensing technology based on the excellent coupling ability of optical fibers, the quantum-enhanced sensing of optical fibers can be achieved (as shown in Table 2, offering benefits compared to traditional methods when it comes to detecting physical parameters like curvature, temperature, and strain force. Additionally, this can also exceed classical techniques in measuring physical quantities that influence the amplitude and phase of the optical field in a fiber). There are also many experiments on quantum-enhanced optical fiber sensing achieved by quantum states injected into optical fiber devices. The Y. Zhao team from Northeastern University conducted salinity measurements and biosensing for protein measurement through optical fiber quantum sensors with quantum state injection into optical fiber devices [138–140]. These research efforts have laid the groundwork for creating sensors with high resolution and sensitivity, showcasing the impressive capabilities of optical fiber quantum sensing systems.

Table 2. The performance metrics of optical fiber quantum sensing technology.

Years	Quantum Devices	Quantum States	Measurement Methods	The Measured Physical Quantity	The Improvement of SNR (SNRI) Compared to SNL
2012 [57]	FOPA	the intensity difference squeezed state 3.1 dB	differential detector	amplitude	
2016 [81]	FOPA	quadrature amplitude entanglement 1 dB/0.8 dB	homodyne detection	noise variances of the difference/sum of the quadrature amplitudes	
2018 [82]	FOPA	the intensity difference squeezed state 6.1 dB	homodyne detection	amplitude	
2020 [84]	FOPA	the intensity difference squeezed state 4.6 dB	PSA-assisted homodyne detection	amplitude	
2023 [83]	FOPA	the intensity difference squeezed state 3.8 dB	differential detector	amplitude	

Table 2. *Cont.*

Years	Quantum Devices	Quantum States	Measurement Methods	The Measured Physical Quantity	The Improvement of SNR (SNRI) Compared to SNL
2023 [88]	FOPA	the intensity-difference squeezed state 2.9 dB		temperature/ curvature	1.1 dB/1.14 dB
2010 [124]	optical Sagnac interferometer	squeezed state injected 6.4 dB		phase	4.5 dB
2018 [108]	NLI based on FOPA	entanglement state		phase amplitude and quadrature components at any angle	20%
2019 [107]	NLI based on FOPA	entanglement state	joint measurement	dual-arm sensing (phase)	3.9 dB
2019 [126]	optical fiber Sagnac interferometer	N00N state injected		phase shift caused by rotational motion	approximately 1.21 dB
2023 [137]	optical fiber MZI	squeezed state injected		phase	3 dB
2025 [127]	optical fiber Sagnac interferometer	generated by FOPA 2.9 dB		strain/curvature	1.54 dB/1.31 dB

However, it is undeniable that the squeezed degree of the quantum states generated by FOPA (or the Kerr effect) still needs an optimization journey when compared to the 15 dB squeezed degree of OPA-based, second-order, nonlinear processes. Optical fibers offer benefits such as lower loss and easier integration with various optical beams for generating and transmitting quantum states. However, phenomena like Brillouin and Raman scattering in optical fibers can hinder advancements in the squeezing of quantum states. Raman scattering and Brillouin scattering are types of non-elastic scattering that occur in optical fibers. In nonlinear processes, when a photon from the pump field is annihilated, it can produce a low-frequency signal photon and a phonon that meets the requirements of momentum and energy conservation. The generation of optical phonons during Raman scattering leads to Raman noise, while the creation of acoustic phonons during Brillouin scattering results in Brillouin noise. For short pulse pumps with a duration of 10 ns or less, Brillouin scattering is minimal. Raman gain depends on the average power of the pump light and is significantly influenced by temperature. Consequently, reducing the temperature of the fiber or using pulsed light pumping can decrease the number of Raman photons. Additionally, achieving a large detuning phase matching that goes beyond the Raman gain spectrum can effectively mitigate or lessen the impact of Raman noise [141]. Certain applications that face environmental interference necessitate a quantum light source with a high degree of squeezing. This presents both opportunities and challenges. We should anticipate advancements in squeezing levels and new applications for quantum light sources based on FOPA or the Kerr effect.

Looking forward to the future, investigating optical fibers made from lower loss materials, such as fluoride optical fibers, could enhance optical fiber sensing. In recent years, optical fibers made from a combination of two-dimensional transition metal dichalcogenides have improved the interaction between light and matter, leading to a remarkable

increase in second harmonic generation [142]. The intensity of the second harmonic has risen by about 300 times compared to single-layer MoS2/silica [143]. These research developments have shown that it is possible to utilize second-order nonlinear effects in optical fibers. Achieving strong second-order nonlinear effects in optical fibers could greatly aid methods for generating quantum states and produce higher-quality quantum resources. The progress of integrated, miniaturized, and scalable quantum sensing platforms relies heavily on optical fiber devices [97]. Optical fiber quantum sensing technology is at the cutting edge of quantum sensing and has the potential to revolutionize precision measurement. Ongoing advancements in system miniaturization, noise reduction, and quantum state manipulation will be crucial for developing ultra-sensitive quantum sensors and advancing the practical application of sensing technologies.

Author Contributions: Conceptualization, X.Z. and B.L.; validation, X.Z., B.L., X.C. and J.S.; formal analysis, X.Z., X.C. and J.S.; investigation, X.Z., Z.T. and B.L.; writing—original draft preparation, X.Z. and Z.T.; writing—review and editing, X.Z. and B.L. All authors have read and agreed to the published version of the manuscript.

Funding: This research was funded by the National Science Foundation of China grant number 62305056, National Key R&D Program of China grant number 2022YFC2204903, Guangdong Provincial Key Laboratory of Advanced Particle Detection Technology grant number 2024B1212010005, the National Natural Science Foundation of China grant number 12227810, the Natural Science Foundation of Guangdong Province grant number 2023A1515011899, Dongguan Science and Technology of Social Development Program grant number 20231800903222, the Dongguan Science and Technology of Social Development Program grant number 20221800905082, Special projects in key fields of colleges and universities in Guangdong Province grant number 2023ZDZX2063.

Institutional Review Board Statement: Not applicable.

Informed Consent Statement: Not applicable.

Data Availability Statement: Data will be made available upon request.

Conflicts of Interest: The authors declare no conflicts of interest.

References

1. Bashan, G.; London, Y.; Diamandi, H.H.; Zadok, A. Distributed cladding mode fiber-optic sensor. *Optica* **2020**, *7*, 85–92. [CrossRef]
2. Tian, J.; Li, Z.; Sun, Y.; Yao, Y. High-sensitivity fiber-optic strain sensor based on the vernier effect and separated Fabry–Perot interferometers. *J. Light. Technol.* **2019**, *37*, 5609–5618. [CrossRef]
3. Du, B.; He, J.; Xu, B.J.; Xu, X.Z.; Fu, C.L.; Li, P.F. High-density weak in-fibermicro-cavity array for distributed high-temperature sensing with millimeter spatial resolution. *J. Light. Technol.* **2022**, *40*, 7447–7455. [CrossRef]
4. Qi, X.G.; Wang, S.; Jiang, J.F.; Liu, K.; Wang, X.; Yang, Y.G. Fiber optic fabry-perot pressure sensor with embedded MEMS micro-cavity for ultra-high pressure detection. *J. Light. Technol.* **2019**, *37*, 2719–2725. [CrossRef]
5. Lu, H.L.; Yue, Y.L.; Jing Du, J.; Shao, L.P.; Wu, T.Y.; Pan, J.; Hu, J.H. Temperature and liquid refractive index sensor using P-D fiber structure-based Sagnac loop. *Opt. Express* **2018**, *26*, 18920–18927. [CrossRef]
6. Ujah, E.; Lai, M.; Slaughter, G. Ultrasensitive tapered optical fiber refractive index glucose sensor. *Sci. Rep.* **2023**, *13*, 4495. [CrossRef]
7. Costa, L.; Martins, H.F.; Martín-López, S.; Fernández-Ruiz, M.R.; González-Herráez, M. Fully distributed optical fiber strain sensor with $10^{-12}\epsilon/\sqrt{\text{Hz}}$ sensitivity. *J. Light. Technol.* **2019**, *37*, 4487–4495. [CrossRef]
8. Dong, S.; Dong, B.; Yu, C.; Guo, Y. High sensitivity optical fiber curvature sensor based on cascaded fiber interferometer. *J. Light. Technol.* **2018**, *36*, 1125–1130. [CrossRef]
9. Wei, Y.; Liu, C.B.; Liu, C.L.; Shi, C.; Wang, R.; Wang, X.K.; Ren, Z.; Ran, Z.; Liu, Z.H.; Zhang, Y. Multi-channel curvature sensor based on fiber bending loss wavelength and SPR. *Opt. Lett.* **2022**, *47*, 6017–6020. [CrossRef]
10. Abbott, B.P.; Abbott, R.; Abbott, T.D.; Abernathy, M.R.; Acernese, F.; Ackley, K.; Adams, C.; Adams, T.; Addesso, P.; Adhikari, R.X.; et al. Observation of Gravitational Waves from a Binary Black Hole Merger. *Phys. Rev. Lett.* **2016**, *116*, 061102. [CrossRef]
11. Abbott, B.P.; Abbott, R.; Abbott, T.D.; Acernese, F.; Ackley, K.; Adams, C.; Adams, T.; Addesso, P.; Adhikari, R.X.; Adya, V.B.; et al. GW170817: Observation of Gravitational Waves from a Binary Neutron Star Inspiral. *Phys. Rev. Lett.* **2017**, *119*, 161101. [CrossRef]

12. Liu, Z.X.; Wang, B.; Kong, C.; Si, L.G.; Xiong, H.; Wu, Y. A proposed method to measure weak magnetic field based on a hybrid optomechanical system. *Sci. Rep.* **2017**, *7*, 12521. [CrossRef]
13. Liu, Z.X.; Xiong, H. Highly sensitive charge sensor based on atom-assisted high-order sideband generation in a hybrid optomechanical system. *Sensors* **2018**, *18*, 3833. [CrossRef] [PubMed]
14. Jing, M.; Hu, Y.; Ma, J.; Zhang, H.; Zhang, L.; Xiao, L.; Jia, T. Atomic super heterodyne receiver based on microwave-dressed Rydberg spectroscopy. *Nat. Phys.* **2020**, *16*, 911–915. [CrossRef]
15. Sewell, R.I.; Koschorreck, M.; Napolitano, M.; Dubost, B.; Behbood, N.; Mitchell, M.W. Magnetic Sensitivity Beyond the Projection Noise Limit by Spin squeezing. *Phy. Rev. Lett.* **2012**, *109*, 253605. [CrossRef] [PubMed]
16. Gross, C.; Zibold, T.; Nicklas, E.; Esteve, J.; Oberthaler, M.K. Nonlinear atom interferometer surpasses classical precision limit. *Nature* **2010**, *464*, 1165. [CrossRef]
17. Anderson, B.E.; Gupta, P.; Schmittberger, B.L.; Horrom, T.; Hermann-Avigliano, C.; Jones, K.M.; Lett, P.D. Phase sensing beyond the standard quantum limit with a variation on the SU(1,1) interferometer. *Optica* **2017**, *4*, 752. [CrossRef]
18. Pooser, R.C.; Lawrie, B. Ultrasensitive measurement of microcantilever displacement below the shot-noise limit. *Optica* **2015**, *2*, 393. [CrossRef]
19. Zuo, X.J.; Yan, Z.H.; Feng, Y.N.; Ma, J.X.; Jia, X.J.; Xie, C.D.; Peng, K.C. Quantum Interferometer Combining Squeezing and Parametric Amplification. *Phys. Rev. Lett.* **2020**, *124*, 173602. [CrossRef]
20. Tse, M.; Yu, H.; Kijbunchoo, N.; Galiana, A.F. Quantum-Enhanced Advanced LIGO Detectors in the Era of Gravitational-Wave Astronomy. *Phys. Rev. Lett.* **2019**, *123*, 231107. [CrossRef]
21. Vahlbruch, H.; Mehmet, M.; Luck, H.; Danzmann, K. Increasing the Astrophysical Reach of the Advanced Virgo Detector via the Application of Squeezed Vacuum States of Light. *Phys. Rev. Lett.* **2019**, *123*, 231108. [CrossRef]
22. Pooser, R.C.; Savino, N.; Batson, E.; Beckey, J.L.; Garcial, J.; Lawrie, B.J. Truncated Nonlinear Interferometry for Quantum-Enhanced Atomic Force Microscopy. *Phys. Rev. Lett.* **2020**, *124*, 230504. [CrossRef] [PubMed]
23. Taylor, M. Biological Measurement Beyond the Quantum Limit. *Nat. Photonics* **2013**, *7*, 229–233. [CrossRef]
24. Vahlbruch, H.; Mehmet, M.; Danzmann, K.; Schnabel, R. Detection of 15 dB Squeezed States of Light and their Application for the Absolute Calibration of Photoelectric Quantum Efficiency. *Phys. Rev. Lett.* **2016**, *117*, 110801. [CrossRef] [PubMed]
25. Zhou, Y.; Yu, J.; Yan, Z.; Jia, X.; Zhang, J.; Xie, C.; Peng, K. Quantum Secret Sharing Among Four Players Using Multipartite Bound Entanglement of an Optical Field. *Phys. Rev. Lett.* **2018**, *121*, 150502. [CrossRef]
26. Larsen, M.V.; Guo, X.S.; Breum, C.R.; Nielsen, J.S.N.; Andersen, U.L. Deterministic generation of a two-dimensional cluster state. *Science* **2019**, *366*, 369. [CrossRef]
27. Kitagawa, M.; Yamamoto, Y. Number-phase minimum-uncertainty state with reduced number uncertainty in a Kerr nonlinear interferometer. *Phys. Rev. A* **1986**, *34*, 3974. [CrossRef]
28. Korolkova, N.; Leuchs, G.; Loudon, R.; Ralph, T.C.; Silberhorn, C. Polarization squeezing and continuous-variable polarization entanglement. *Phys. Rev. A* **2002**, *65*, 052306. [CrossRef]
29. Silberhorn, C.; Lam, P.K.; Weiss, O.; König, F.; Korolkova, N.; Leuchs, G. Generation of Continuous Variable Einstein-Podolsky-Rosen Entanglement via the Kerr Nonlinearity in an Optical Fiber. *Phys. Rev. Lett.* **2001**, *86*, 4267. [CrossRef]
30. Peng, Y.; Zhao, Y.; Chen, M.Q.; Xia, F. Research Advances in Microfiber Humidity Sensors. *Small* **2018**, *14*, 1800524. [CrossRef]
31. Cheol, J.; Shin, M.; Han, Y.G. Relative Humidity Sensor Based on an Optical Microfiber Knot Resonator with a Polyvinyl Alcohol Overlay. *J. Light. Technol.* **2016**, *34*, 4511. [CrossRef]
32. Bo, L.; Wang, P.; Semenova, Y.; Farrell, G. Optical microfiber coupler based humidity sensorwith a polyethylene oxide coating. *Microw. Opt. Technol. Lett.* **2015**, *57*, 457–460. [CrossRef]
33. Tan, Y.; Sun, L.P.; Jin, L.; Li, J.; Guan, B. Microfiber Mach-Zehnder interferometer based on long period grating for sensing applications. *Opt. Express* **2013**, *21*, 154–164. [CrossRef]
34. Wu, Q.; Semenova, Y.; Wang, P.; Farrell, G. High sensitivity SMS fiber structure based refractometer–analysis and experiment. *Opt. Express* **2011**, *19*, 7937–7944. [CrossRef] [PubMed]
35. Gao, H.; Hu, H.; Zhao, Y.; Li, J.; Lei, M.;Zhang, Y. Highly-sensitive optical fiber temperature sensors based on PDMS/silica hybrid fiber structures. *Sens. Actuators A Phys.* **2018**, *284*, 22–27. [CrossRef]
36. Eberle, T.; Steinlechner, S.; Bauchrowitz, J.; Handchen, V.; Vahlbruch, H.; Mehmet, M.; Muller-Ebhardt, H.; Schnabe, R. Quantum Enhancement of the Zero-area Sagnac Interferometer Topology for Gravitational Wave Detection. *Phys. Rev. Lett.* **2010**, *104*, 251102. [CrossRef] [PubMed]
37. Xin, Y.; Dong, X.; Meng, Q.; Qi, F.; Zhao, C.L. Alcohol-filled side-hole fiber Sagnac interferometer for temperature measurement. *Sens. Actuators A Phys.* **2013**, *193*, 182–185. [CrossRef]
38. Zhao, N.; Fu, H.; Shao, M.; Yan, X.; Li, H.D.; Liu, Q.P.; Gao, H.; Liu, Y.G.; Qiao, X.G. High temperature probe sensor with high sensitivity based on Michelson interferometer. *Opt. Commun.* **2015**, *343*, 131–134. [CrossRef]
39. Goda, K.; Miyakawa, O.; Mikhailov, E.E.; Saraf, S.; Adhikari, R.; McKenzie, K.; Ward, R.; Vass, S.; Weinstein, A.J.; Mavalvala, N. A quantum-enhanced prototype gravitational-wave detector. *Nat. Phys.* **2008**, *4*, 472. [CrossRef]

40. Xin, Y.; Zhao, M.; Zhao, H.; Gong, H.P.; Shen, C.Y.; Zhao, C.L.; Dong, X.Y. Alcohol-filled side-hole fiber based Mach-Zehnder interferometer for temperature measurement. *Opt. Fiber Technol.* **2018**, *46*, 72–76. [CrossRef]
41. Xu, C.; Zhang, L.; Huang, S.; Ma, T.; Liu, F.; Yonezawa, H.; Zhang, Y.; Xiao, M. Sensing and tracking enhanced by quantum squeezing. *Photonics Res.* **2019**, *7*, 6. [CrossRef]
42. Hoff, U.B.; Harris, G.I.; Madsen, L.S.; Kerdoncuff, H.; Lassen, M.; Kerdoncuff, H.; Lassen, M.; Nielsen, B.M.; Bowen, W.P.; Andersen, U.L. Quantum-enhanced micro-mechanical displacement sensitivity. *Opt. Lett.* **2013**, *38*, 1413. [CrossRef] [PubMed]
43. Xiao, M.; Wu, L.A.; Kimble, H.J. Precision measurement beyond the shot-noise limit. *Phys. Rev. Lett.* **1987**, *59*, 278. [CrossRef] [PubMed]
44. O'brien, J.L.; Furusawa, A.; Vučković, J. Photonic quantum technologies. *Nat. Photonics* **2009**, *3*, 687–695. [CrossRef]
45. Huo, M.R.; Qin, J.L.; Cheng, J.L.; Yan, Z.H.; Qin, Z.Z.; Su, X.L.; Jia, X.J.; Xie, C.D.; Peng, K.C. Deterministic quantum teleportation through fiber channels. *Sci. Adv.* **2018**, *4*, eaas9401. [CrossRef]
46. Liang, S.C.; Cheng, J.L.; Qin, J.L.; Li, J.T.; Shi, Y.; Yan, Z.H.; Jia, X.J.; Xie, C.D.; Peng, K.C. High-speed quantum radio-frequency-over-light communication. *Phys. Rev. Lett.* **2024**, *132*, 140802. [CrossRef]
47. Clark, J.B.; Lecocq, F.; Simmonds, R.W.; Aumentado, J.; Teufel, J.D. Observation of strong radiation pressure forces from squeezed light on a mechanical oscillator. *Nat. Phys.* **2016**, *12*, 683. [CrossRef]
48. Li, B.B.; Bilek, J.; Hoff, U.B.; Madsen, L.S.; Forstner, S. Quantum enhanced optomechanical magnetometry. *Optics* **2018**, *5*, 850. [CrossRef]
49. Heersink, J.; Gaber, T.; Lorenz, S.; Glockl, O.; Korolkova, N.; Leuchs, G. Polarization squeezing of intense pulses with a fiber optic Sagnac interferometer. *Phys. Rev. A* **2003**, *68*, 013815. [CrossRef]
50. Barreiro, S.; Valente, P.; Failache, H.; Lezama, A. Polarization squeezing of light by single passage through an atomic vapor. *Phys. Rev. A* **2011**, *84*, 033851. [CrossRef]
51. Su, X.; Zhao, Y.; Hao, S.; Xie, C.; Peng, K. Experimental preparation of eight-partite cluster state for photonic qumodes. *Opt. Lett.* **2012**, *37*, 5178. [CrossRef] [PubMed]
52. Shi, S.P.; Wang, Y.J.; Yang, W.H.; Zheng, Y.H.; Peng, K.C. Detection and perfect fitting of 13.2 dB squeezed vacuum states by considering green-light-induced infrared absorption. *Opt. Lett.* **2018**, *43*, 5411. [CrossRef] [PubMed]
53. Morin, O.; Huang, K.; Liu, J.; Jeannic, H.L.; Fabre, C.; Laurat, J. Remote creation of hybrid entanglement between particle-like and wave-like optical qubits. *Nat. Photonics* **2014**, *8*, 570–574. [CrossRef]
54. Eberle, T.; Handchen, V.; Schnabel, R. Stable control of 10 dB two-mode squeezed vacuum states of light. *Opt. Express* **2013**, *21*, 11546–11553. [CrossRef]
55. Zhang, J.; Peng, K.C. Quantum teleportation and dense coding by means of bright amplitude-squeezed light and direct measurement of a Bell state. *Phys. Rev. A* **2000**, *62*, 064302. [CrossRef]
56. Sharping, J.E.; Fiorentino, M.; Kumar, P. Observation of twin-beam-type quantum correlation in optical fiber. *Opt. Lett.* **2001**, *26*, 367–369. [CrossRef]
57. Guo, X.S.; Li, X.Y.; Liu, N.N.; Yang, L.; Ou, Z.Y. An all-fiber source of pulsed twin beams for quantum communication. *Appl. Phys. Lett.* **2012**, *101*, 261111. [CrossRef]
58. Brida, G.; Genovese, M.; Berchera, I.R. Experimental realization of sub-shot-noise quantum imaging. *Nat. Photonics* **2010**, *4*, 227–230. [CrossRef]
59. Lunghi, T.; Brask, J.B.; Lim, C.C.W.; Lavigne, Q.; Bowles, J.; Martin, A.; Zbinden, H.; Brunner, N. Self-testing quantum random number generator. *Phys. Rev. Lett.* **2015**, *114*, 150501. [CrossRef]
60. Zhang, Q.; Deng, X.W.; Tian, C.X.; Xiao, L.S. Quantum random number generator based on twin beams. *Opt. Lett.* **2017**, *42*, 895–898. [CrossRef]
61. Hald, J.; Sorensen, J.L.; Schori, C.; Polzik, E.S. Spin squeezed atoms: A new sub-Poissonian atomic beam. *J. Mod. Opt.* **2001**, *47*, 2599–2603. [CrossRef]
62. Wolfgramm, F.; Cere, A.; Beduini, F.A.; Predojevic, A.; Koschorreck, M.; Mitchell, M.W. Squeezed-Light Optical Magnetometry. *Phys. Rev. Lett.* **2010**, *105*, 053601. [CrossRef]
63. Bai, L.L.; Zhang, L.L.; Yang, Y.B.; Chuang, R.; Qin, Y.; He, J.; Wen, X.; Wang, J.M. Enhancement of spin noise spectroscopy of rubidium atomic ensemble by using the polarization squeezed light. *Opt. Express* **2022**, *30*, 1925–1935. [CrossRef]
64. Wu, L.; Yan, Z.H.; Liu, Y.H.; Deng, R.J.; Jia, X.J.; Xie, C.D.; Peng, K.C. Experimental generation of tripartite polarization entangled states of bright optical beams. *Appl. Phys. Lett.* **2016**, *108*, 161102. [CrossRef]
65. Josse, V.; Dantan, A.; Bramati, A.; Pinard, M.; Giacobino, E. Continuous variable entanglement using cold atoms. *Phys. Rev. Lett.* **2014**, *92*, 123601. [CrossRef] [PubMed]
66. Korolkova, N.; Loudon, R.; Leuchs, G. Nonseparability and squeezing of continuous polarization variables. *Phys. Rev. A* **2005**, *71*, 032343. [CrossRef]
67. Hudelist, F.; Kong, J.; Liu, C.J.; Jing, J.T.; Ou, Z.Y.; Zhang, W.P. Quantum metrology with parametric amplifier-based photon correlation interferometers. *Nat. Commun.* **2014**, *5*, 3049. [CrossRef]

68. Du, W.; Wu, S.H.; Zhang, D.; Chen, J.; Yang, Y.Q.; Yang, P.Y.; Guo, J.X.; Bao, G.Z.; Zhang, W.P. Quantum Twin Interferometers. *arXiv* **2025**, arXiv:2501.04244. [CrossRef]
69. Li, J.; Liu, Y.; Cui, L.; Huo, N.; Assad, S.M.; Li, X.; Ou, Z.Y. Joint measurement of multiple noncommuting parameters. *Phys. Rev. A* **2018**, *97*, 052127. [CrossRef]
70. Guo, X.S.; Li, X.Y.; Liu, N.N.; Ou, Z.Y. Multimode theory of pulsed-twin-beams generation from a high-gain fiber-optical parametric amplifier. *Phys. Rev. A* **2013**, *88*, 023841. [CrossRef]
71. Sharping, J.E.; Chen, J.; Li, X.Y.; Kumar, P. Quantum-correlated twin photons from microstructure fiber. *Opt. Express* **2004**, *12*, 3086–3094. [CrossRef]
72. Takesue, H.; Inoue, K. 1.5-m band quantum-correlated photon pair generation in dispersionshifted fiber: Suppression of noise photons by cooling fiber. *Opt. Express* **2005**, *13*, 7832–7839. [CrossRef] [PubMed]
73. Patel, M.; Altepeter, J.B.; Huang, Y.P.; Oza, N.N.; Prem Kumar, P. Independent telecom-fiber sources of quantum indistinguishable single photons. *New J. Phys.* **2014**, *16*, 043019. [CrossRef]
74. Zhu, F.; Zhang, W.; Huang, Y. Fiber-based frequency-degenerate polarization entangled photon pair sources for information encoding. *Opt. Express* **2016**, *24*, 25619–25628. [CrossRef] [PubMed]
75. Shelby, R.M.; Levenson, M.D.; Perlmutter, S.H.; DeVoe, R.G.; Walls, D.F. Broad-band parametric deamplification of quantum noise in an optical fiber. *Phys. Rev. Lett.* **1986**, *57*, 691–694. [CrossRef]
76. Li, X.Y.; Yang, L.; Ma, X.X.; Cui, L.; Ou, Z.Y.; Yu, D.Y. All-fiber source of frequency-entangled photon pairs. *Phys. Rev. A* **2009**, *79*, 033817. [CrossRef]
77. Li, X.Y.; Ma, X.X.; Quan, L.M.; Yang, L.; Cui, L.; Guo, X.S. Quantum efficiency measurement of single-photon detectors using photon pairs generated in optical fibers. *J. Opt. Soc. Am. B* **2010**, *27*, 1857–1865. [CrossRef]
78. Yang, L.; Ma, X.X.; Guo, X.S.; Cui, L.; Li, X.Y. Characterization of a fiber-based source of heralded single photons. *Phys. Rev. A* **2011**, *83*, 053843. [CrossRef]
79. Zhou, Q.; Zhang, W.; Cheng, J.R.; Huang, Y.D.; Peng, J.D. Noise performance comparison of 1.5 μm correlated photon pair generation in different fibers. *Opt. Express* **2010**, *18*, 17114–17123. [CrossRef]
80. Zhou, Q.; Zhang, W.; Cheng, J.R.; Huang, Y.D.; Peng, J.D. Polarization-entangled Bell states generation based on birefringence in high nonlinear microstructure fiber at 1.5 μm. *Opt. Lett.* **2009**, *34*, 2706–2708. [CrossRef]
81. Guo, X.S.; Liu, N.N.; Liu, Y.H.; Li, X.Y.; Ou, Z.Y. Generation of continuous variable quantum entanglement using a fiber optical parametric amplifier. *Opt. Lett.* **2016**, *41*, 653. [CrossRef]
82. Liu, Y.H.; Huo, N.; Li, J.M.; Li, X.Y. Long-distance distribution of the telecom band intensity difference squeezing generated in a fiber optical parametric amplifier. *Opt. Lett.* **2018**, *43*, 5559–5562. [CrossRef] [PubMed]
83. Zhao, W.; Guo, X.S.; Li, X.Y. Time-domain measurement of twin beams produced by fiber amplifiers with an ultra-fast pulse train as a pump. *Opt. Lett.* **2023**, *48*, 444–447. [CrossRef] [PubMed]
84. Li, J.M.; Liu, Y.H.; Huo, N.; Cui, L.; Feng, S.; Li, X.Y.; Ou, Z.Y. Measuring the continuous variable quantum entanglement with a parametric amplifier assisted homodyne detection. *Phys. Rev. A* **2020**, *101*, 053801. [CrossRef]
85. Kong, J.; Hudelist, F.; Ou, Z.Y.; Zhang, W. Cancellation of internal quantum noise of an amplifier by quantum correlation. *Phys. Rev. Lett.* **2013**, *111*, 033608. [CrossRef]
86. Guo, X.S.; Li, X.Y.; Liu, N.N.; Ou, Z.Y. Quantum information tapping using a fiber optical parametric amplifier with noise figure improved by correlated inputs. *Sci. Rep.* **2016**, *6*, 30214. [CrossRef]
87. Kong, J.; Ou, Z.Y.; Zhang, W.P. Phase-measurement sensitivity beyond the standard quantum limit in an interferometer consisting of a parametric amplifier and a beam splitter. *Phys. Rev. A* **2013**, *87*, 023825. [CrossRef]
88. Wang, H.L.; Shi, Y.P.; Fu, Z.X.; Chen, Z.H.; Jin, S.Z.; Zhao, C.L. Experimental implementation of quantum-enhanced tapered fiber sensor for simultaneous measurement of curvature and temperature. *Opt. Fiber Technol.* **2023**, *81*, 103545. [CrossRef]
89. Rosenbluh, M.; Shelby, R.M. Squeezed optical solitons. *Phys. Rev. Lett.* **1991**, *66*, 153–156. [CrossRef]
90. Schmitt, S.; Ficker, J.; Wolff, M.; Konig, F.; Sizmann, A.; Leuchs, G. Photon-number-squeezed solitons from an asymmetric fiber-optic Sagnac interferometer. *Phys. Rev. Lett.* **1998**, *81*, 2446–2449. [CrossRef]
91. Hirosawa, K.; Furumochi, H.; Tada, A.; Kannari, F.; Takeoka, M.; Sasaki, M. Photon number squeezing of ultrabroadband laser pulses generated by microstructure fibers. *Phys. Rev. Lett.* **2005**, *94*, 203601. [CrossRef]
92. Heersink, J.; Josse, V.; Leuchs, G.; Andersen, U.L. Efficient polarization squeezing in optical fibers. *Opt. Lett.* **2005**, *30*, 1192–1194. [CrossRef] [PubMed]
93. Corney, J.F.; Drummond, P.D.; Heersink, J.; Josse, V.; Leuchs, G.; Andersen, U.L. Many-body quantum dynamics of polarization squeezing in optical fibre. *Phys. Rev. Lett.* **2006**, *97*, 023606. [CrossRef] [PubMed]
94. Corney, J.F.; Heersink, J.; Dong, R.; Josse, V.; Drummond, P.D.; Leuchs, G.; Andersen, U.L. Simulations and experiments on polarization squeezing in optical fiber. *Phys. Rev. A* **2008**, *78*, 023831. [CrossRef]
95. Rigas, I.; Klimov, A.B.; Sanchez-Soto, L.L.; Leuchs, G. Nonlinear cross-Kerr quasiclassical dynamics. *New J. Phys.* **2013**, *15*, 043038. [CrossRef]

96. Dong, R.; Heersink, J.; Corney, J.F.; Drummond, P.D.; Andersen, U.L.; Leuchs, G. Experimental evidence for Raman-induced limits to efficient squeezing in optical fibers. *Opt. Lett.* **2008**, *33*, 116–118. [CrossRef]
97. Kaiser, F.; Fedrici, B.; Zavatta, A.; dAuria, V.; Tanzilli, S. A fully guided-wave squeezing experiment for fiber quantum networks. *Optica* **2016**, *3*, 362–365. [CrossRef]
98. Mondain, F.; Lunghi, T.; Zavatta, A.; Gouzien, E.; Doutre, F.; De Micheli, M.; Tanzilli, S.; D'Auria, V. Chip-based squeezing at a telecom wavelength. *Photonics Res.* **2019**, *7*, 36–39. [CrossRef]
99. Taylor, M.A.; Janousek, J.; Daria, V.; Knittel1, J.; Hage, B.; Bachor, H.A.; Bowen, W.P. Subdiffraction-Limited Quantum Imaging within a Living Cell. *Phys. Rev. X* **2014**, *4*, 011017. [CrossRef]
100. Mason, D.; Chen, J.X.; Rossi, M.; Tsaturyan, Y.; Schliesser, A. Continuous force and displacement measurement below the standard quantum limit. *Nat. Phys.* **2019**, *15*, 745. [CrossRef]
101. Xiang, G.Y.; Higgins, B.L.; Berry, D.W.; Wiseman, H.M.; Pryde, G.J. Entanglement-enhanced measurement of a completely unknown optical phase. *Nat. Photonics* **2011**, *5*, 43. [CrossRef]
102. Liu, J.; Liu, W.; Li, S.; Wei, D.; Gao, H.; Li, F. Enhancement of the angular rotation measurement sensitivity based on SU(2) and SU(1,1) interferometers. *Photonics Res.* **2017**, *5*, 617. [CrossRef]
103. Ou, Z.Y. Enhancement of the phase-measurement sensitivity beyond the standard quantum limit by a nonlinear interferometer. *Phys. Rev. A* **2012**, *85*, 023815. [CrossRef]
104. Yurke, B.; McCall, S.L.; Klauder, J.R. SU(2) and SU(1,1) interferometers. *Phys. Rev. A* **1986**, *33*, 4033–4054. [CrossRef]
105. Manceau, M.; Leuchs, G.; Khalili, F.; Chekhova, M. Detection loss tolerant supersensitive phase measurement with an SU(1,1) interferometer. *Phys. Rev. Lett.* **2017**, *119*, 223601. [CrossRef]
106. Du, W.; Jia, J.; Chen, J.F.; Ou, Z.Y.; Jing, J.T. Absolute sensitivity of phase measurement in an SU(1,1) type interferometer. *Opt. Lett.* **2018**, *43*, 1051–1054. [CrossRef] [PubMed]
107. Liu, Y.H.; Huo, N.; Li, J.M.; Cui, L.; Li, X.Y.; Ou, Z.Y. Optimum quantum resource distribution for phase measurement and quantum information tapping in a dual-beam SU(1,1) interferometer. *Opt. Express* **2019**, *27*, 11292. [CrossRef] [PubMed]
108. Liu, Y.H.; Li, J.M.; Cui, L.; Huo, N.; Assad, S.M.; Li, X.Y.; Ou, Z.Y. Loss-tolerant quantum dense metrology with SU(1,1) interferometer. *Opt. Express* **2018**, *26*, 27705. [CrossRef] [PubMed]
109. Flurin, E.; Roch, N.; Mallet, F.; Devoret, M.H.; Huard, B. Generating entangled microwave radiation over two transmission lines. *Phys. Rev. Lett.* **2012**, *109*, 183901. [CrossRef]
110. Linnemann, D.; Strobel, H.; Muessel, W.; Schulz, J.; Lewis-Swan, R.J.; Kheruntsyan, K.V.; Oberthaler, M.K. Quantum-enhanced sensing based on time reversal of nonlinear dynamics. *Phys. Rev. Lett.* **2016**, *117*, 013001. [CrossRef]
111. Cheung, H.F.; Patil, Y.S.; Chang, L.; Chakram, S.; Vengalattore, M. Nonlinear phonon interferometry at the Heisenberg limit. *arXiv* **2016**, arXiv:1601.02324. [CrossRef]
112. Chen, B.; Qiu, C.; Chen, S.Y.; Guo, J.X.; Chen, L.Q.; Ou, Z.Y.; Zhang, W.P. Atom-light hybrid interferometer. *Phys. Rev. Lett.* **2015**, *115*, 043602. [CrossRef]
113. Grace, M.R.; Gagatsos, C.N.; Zhuang, Q.; Guha, S. Quantum-enhanced fiber-optic gyroscopes using quadrature squeezing and continuous-variable entanglement. *Phys. Rev. Appl.* **2020**, *14*, 034065. [CrossRef]
114. Schubert, C.; Abend, S.; Gersemann, M.; Gebbe, M.; Schlippert, D.; Berg, P.; Rasel, E.M. Multi-loop atomic Sagnac interferometry. *Sci. Rep.* **2021**, *11*, 16121. [CrossRef]
115. Zhang, W.X.; Zhang, R.; Zuo, Y.L.; Kuang, L.M. Enhancing the sensitivity of quantum fiber-optical gyroscopes via a non-Gaussian-state probe. *Adv. Quantum Technol.* **2025**, *8*, 2400270. [CrossRef]
116. Krylov, D.; Bergman, K. Amplitude-squeezed solitons from an asymmetric fiber interferometer. *Opt. Lett.* **1998**, *23*, 1390. [CrossRef]
117. Pizzaia, J.P.L.; Castellani, C.E.S.; Leal-Junior, A.G. Highly sensitive temperature sensing based on a birefringent fiber Sagnac loop. *Opt. Fiber Technol.* **2022**, *72*, 102949. [CrossRef]
118. Liu, Q.; Li, S.; Chen, H. Enhanced sensitivity of temperature sensor by a PCF with a defect core based on Sagnac interferometer. *Sens. Actuators B Chem.* **2018**, *254*, 636–641. [CrossRef]
119. Liu, Q.; Xing, L.; Wu, Z.X.; Cai, L.; Zhang, Z.; Zhao, J.C. High-sensitivity photonic crystal fiber force sensor based on Sagnac interferometer for weighing. *Opt. Laser Technol.* **2020**, *123*, 105939. [CrossRef]
120. Zhang, S.Q.; Cao, Z.; Xia, T.T.; Yang, C.K.; Liu, Z.Y.; Li, Z.H. Lateral force sensing based on Sagnac interferometry realized by a high-birefringence suspended-core fiber. *J. Light. Technol.* **2022**, *40*, 3935–3941. [CrossRef]
121. Li, X.G.; Nguyen, L.V.; Zhao, Y.; Ebendorff-Heidepriem, H.; Warren-Smith, S.C. High-sensitivity Sagnac-interferometer biosensor based on exposed core microstructured optical fiber. *Sens. Actuators B Chem.* **2018**, *269*, 103–109. [CrossRef]
122. Huang, B.S.; Sheng, X.; Gao, J.Q.; Gao, W.; Lou, S.Q. High sensitivity twist sensor based on suspended core fiber Sagnac interferometer with temperature calibration. *Opt. Express* **2023**, *31*, 38205. [CrossRef]

123. Han, T.T.; Liu, Y.G.; Wang, Z.; Guo, J.Q.; Wu, Z.F.; Wang, S.X.; Li, Z.L.; Zhou, W.Y. Unique characteristics of a selective-filling photonic crystal fiber Sagnac interferometer and its application as high sensitivity sensor. *Opt. Express* **2013**, *21*, 122–128. [CrossRef]
124. Mehmet, M.; Eberle, T.; Steinlechner, S.; Vahlbruch, H.; Schnabel, R. Demonstration of a quantum-enhanced fiber Sagnac interferometer. *Opt. Lett.* **2010**, *35*, 1665–1667. [CrossRef]
125. Xin, J.; Liu, J.M.; Jing, J.T. Nonlinear Sagnac interferometer based on the four-wave mixing process. *Opt. Express* **2017**, *25*, 1350–1357. [CrossRef]
126. Fink, M.; Steinlechner, F.; Handsteiner, J.; Dowling, J.P.; Scheidl, T.; Ursin, R. Entanglement-enhanced optical gyroscope. *New J. Phys.* **2019**, *21*, 053010. [CrossRef]
127. Wang, H.L.; Chen, Z.H.; Ma, S.Y.; Wang, D.X.; Mao, T.H.; Zhang, Y.; Zhao, C.L. Quantum-Enhanced Strain and Curvature Sensing Based on a Birefringent Fiber Sagnac Interferometer. *J. Light. Technol.* **2025**, *43*, 966. [CrossRef]
128. Duan, D.W.; Rao, Y.J.; Xu, L.C.; Zhu, T.; Wu, D.; Yao, J. In-fiber Mach–Zehnder interferometer formed by large lateral offset fusion splicing for gases refractive index measurement with high sensitivity. *Sens. Actuators B Chem.* **2011**, *160*, 1198–1202. [CrossRef]
129. Jiang, L.; Yang, J.; Wang, S.; Li, B.; Wang, M. Fiber Mach–Zehnder interferometer based on microcavities for high-temperature sensing with high sensitivity. *Opt. Lett.* **2011**, *36*, 3753–3755. [CrossRef] [PubMed]
130. Li, E. Temperature compensation of multimode-interference-based fiber devices. *Opt. Lett.* **2007**, *32*, 2064. [CrossRef]
131. Tripathi, S.M.; Kumar, A.; Varshney, R.K.; Kumar, Y.B.P.; Marin, E.; Meunier, J.P. Strain and temperature sensing characteristics of single-mode-multimode-single-mode structures. *J. Light. Technol.* **2009**, *27*, 2348–2356. [CrossRef]
132. Wu, Q.; Semenova, Y.; Yan, B.B.; Ma, Y.Q.; Wang, P.F.; Yu, C.X.; Farrell, G. Fiber refractometer based on a fiber Bragg grating and single-mode-multimode-single-mode fiber structure. *Opt. Lett.* **2011**, *36*, 2197–2199. [CrossRef]
133. Tian, Z.; Yam, S.S.H. In-line single-mode optical fiber interferometric refractive index sensors. *J. Light. Technol.* **2009**, *27*, 2296–2306. [CrossRef]
134. Lu, P.; Men, L.Q.; Sooley, K.; Chen, Q.Y. Tapered fiber Mach-Zehnder interferometer for simultaneous measurement of refractive index and temperature. *Appl. Phys. Lett.* **2009**, *94*, 131110. [CrossRef]
135. Wang, Q.; Wei, W.Q.; Guo, M.J.; Zhao, Y. Optimization of cascaded fiber tapered Mach-Zehnder interferometer and refractive index sensing technology. *Sens. Actuators B Chem.* **2016**, *222*, 159. [CrossRef]
136. Liu, F.; Zhou, Y.; Yu, J.; Guo, J.; Wu, Y.; Xiao, S.; Wei, D.; Zhang, Y.; Jia, X.; Xiao, M. Squeezing-enhanced fiber Mach-Zehnder interferometer for low-frequency phase measurement. *Appl. Phys. Lett.* **2017**, *110*, 021106. [CrossRef]
137. Kang, G.H.; Feng, J.X.; Cheng, L.; Li, Y.J.; Zhang, K.S. Quantum-enhanced optical precision measurement assisted by low-frequency squeezed vacuum states. *Chin. Phys. B* **2023**, *32*, 104204. [CrossRef]
138. Zhao, Y.; Peng, Y.; Hua, X.G.; Xia, F.; Zhao, Q. Beating the shot-noise limit with optical fiber quantum sensors for salinity measurement. *Sens. Actuators B Chem.* **2020**, *320*, 128353 [CrossRef]
139. Peng, Y.; Zhao, Y.; Hu, X.G.; Yang, Y. Optical fiber quantum biosensor based on surface plasmon polaritons for the label-free measurement of protein. *Sens. Actuators B Chem.* **2020**, *316*, 128097. [CrossRef]
140. Peng, Y.; Zhao, Y. Microfiber quantum sensors for protein measurement with quantum N00N state. *Sens. Actuators B Chem.* **2023**, *383*, 133616. [CrossRef]
141. Alibart, O.; Fulconis, J.; Wong, G.K.L.; Murdoch, S.G.; Wadsworth, W.J.; Rarity, J.G. Photon pair generation using four-wave mixing in a microstructured fibre: Theory versus experiment. *New J. Phys.* **2006**, *8*, 67. [CrossRef]
142. Chen, J.H.; Tan, J.; Wu, G.X.; Zhang, X.J.; Xu, F.; Lu, Y.Q. Tunable and enhanced light emission in hybrid WS2-optical-fiber-nanowire structures. *Light Sci. Appl.* **2019**, *8*, 8. [CrossRef]
143. Zuo, Y.G.; Yu, W.T.; Liu, C.; Cheng, X.; Qiao, R.X.; Liang, J.; Zhou, X.; Wang, J.H.; Wu, M.H.; Zhao, Y.; et al. Optical fibres with embedded two-dimensional materials for ultrahigh nonlinearity. *Nat. Nanotechnol.* **2020**, *15*, 987. [CrossRef]